Supplementary Information

Halide Insertion Regulation for Efficient and Stable Wide-Bandgap Perovskite Photovoltaics

Zexin Song[1]†, Ni Meng[1]†, Yimeng Tian[1]†, Jiwei Li[1], Huiyang Ye[1], Anming Mo[1], Changjiu Sun[1], Zhiqiang Li[1], Shaopeng Yang[1], Tingwei He (何庭伟)[1,2,3]*

[1] Province-Ministry Co-construction Collaborative Innovation Center of Hebei Photovoltaic Technology, Hebei Key Laboratory of Optic-electronic Information and Materials, College of Physics Science and Technology, Hebei University, Baoding 071002, Hebei, China

[2] Institute of Life Science and Green Development, Hebei University, Baoding 071002, China

[3] Key Laboratory of Advanced Energy Materials Chemistry (Ministry of Education), Nankai University, Tianjin 300071, China

* The corresponding authors, E-mail: htw2022@hbu.edu.cn

† These authors contributed equally.

Table of contents

Supplementary Figures

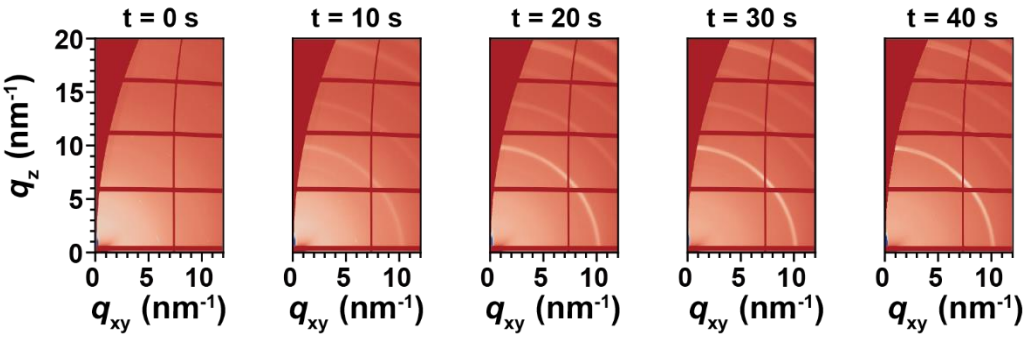

Supplementary Fig. 1 | *In-situ* GIWAXS patterns of control perovskite films.

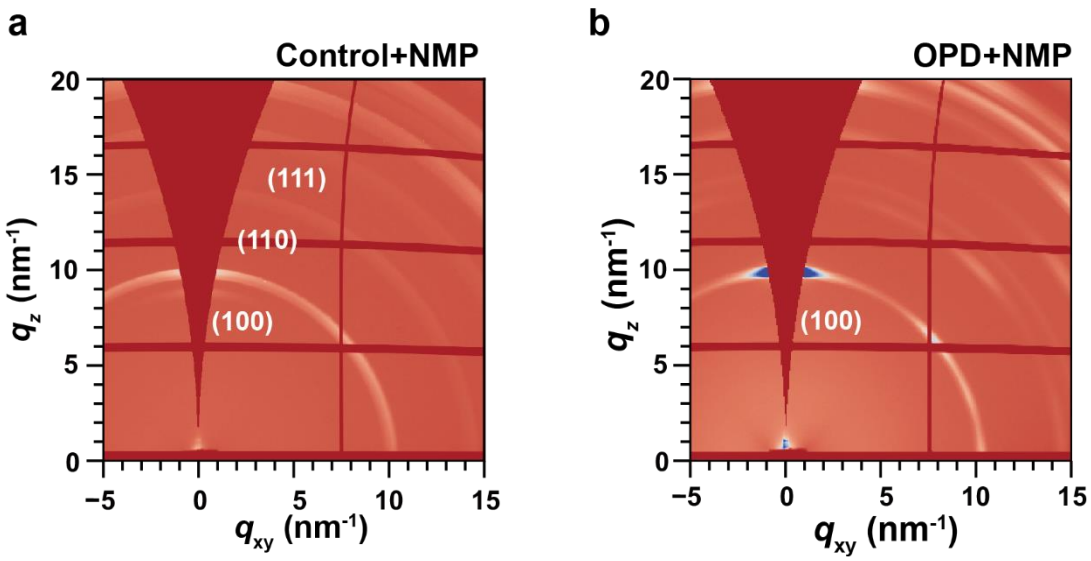

Supplementary Fig. 2 | GIWAXS patterns of (**a)** control and **(b)** OPD-treated perovskite film with NMP solvent (25 V%).

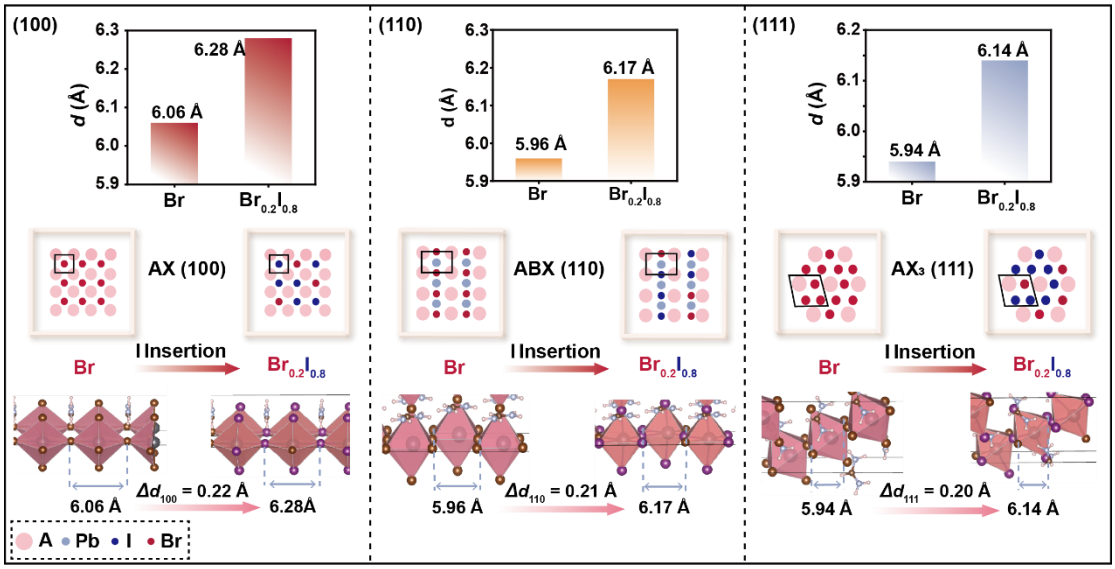

Supplementary Fig. 3 | Perovskite crystal models and DFT-calculated interplanar spacings of (100), (110), and (111) facets before and after random I insertion.

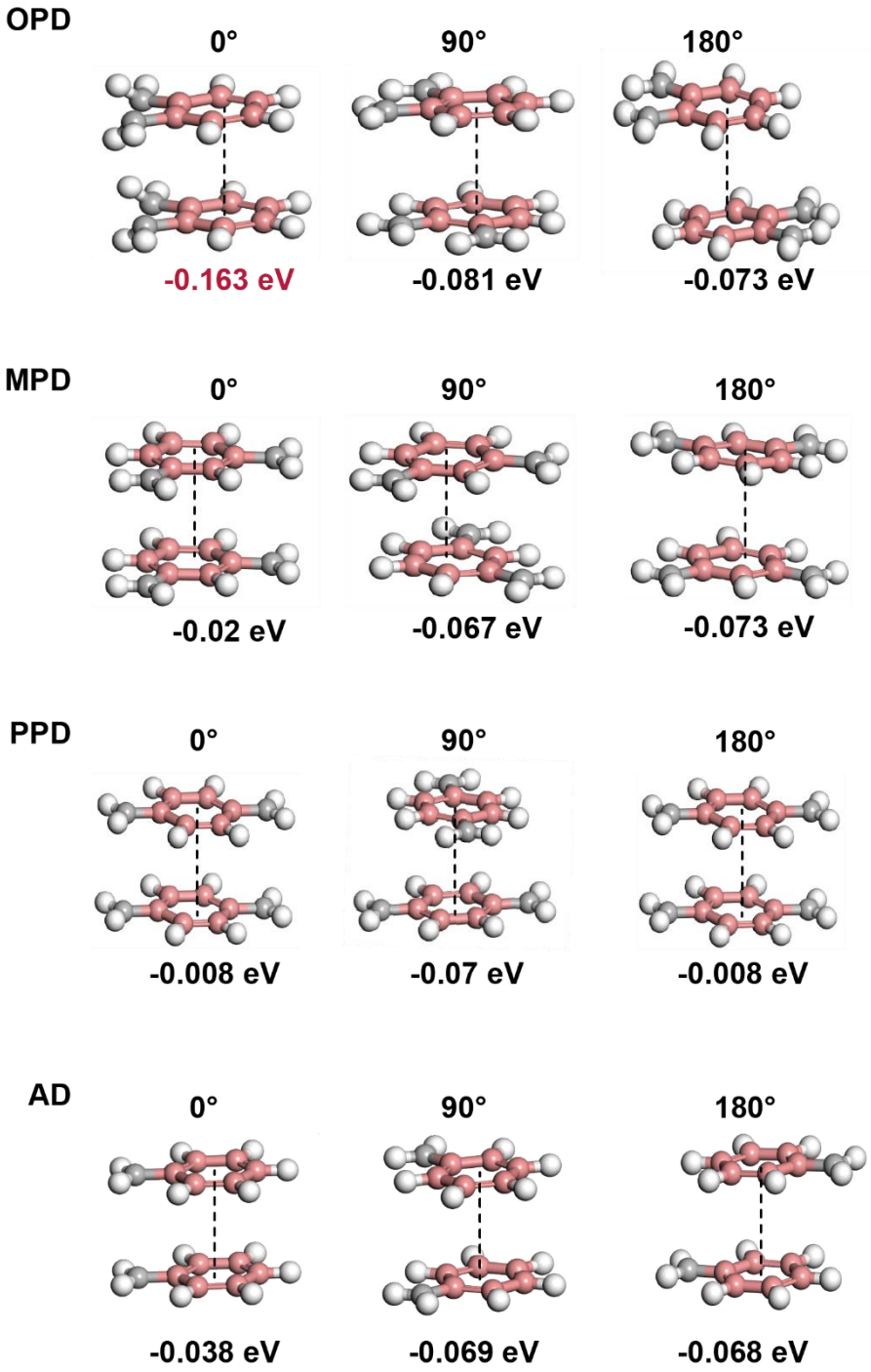

Supplementary Fig. 4 | Stacking modes for OPD, MPD, PPD, and AD used in DFT simulation calculations.

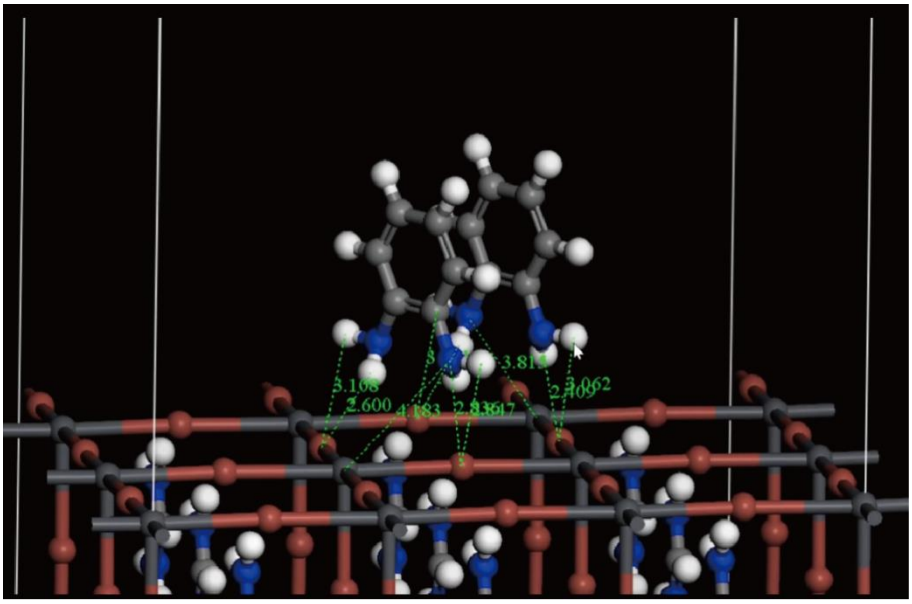

Supplementary Fig. 5 | Strong anchoring effect of OPD parallel stacking on perovskite.

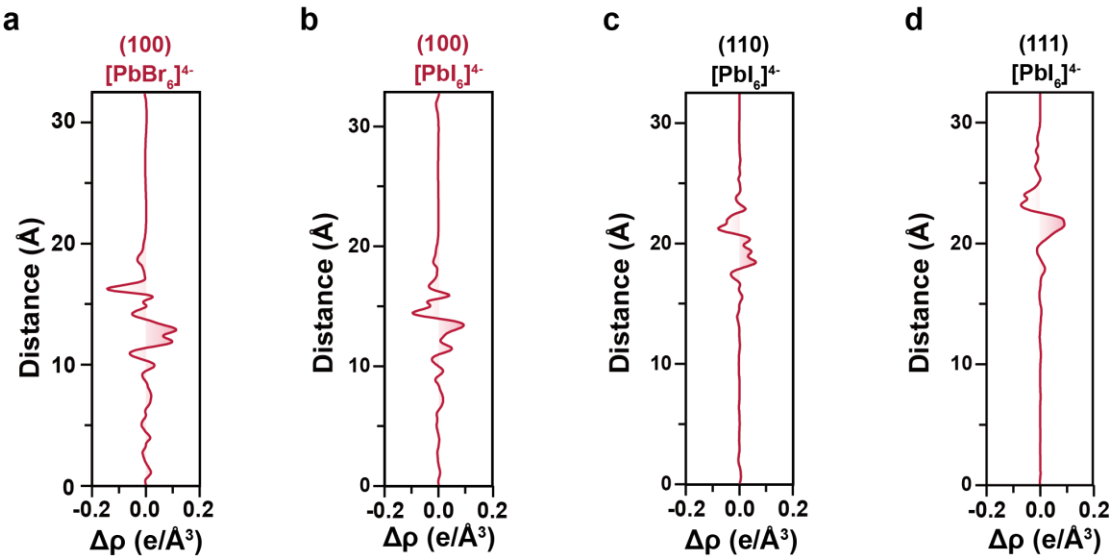

Supplementary Fig. 6 | Longitudinal integral curves of differential charge density after OPD-treated for **(a), (b)** $[PbBr_6]^{4-}$ and $[PbI_6]^{4-}$ under the (100) facet and **(c), (d)** $[PbI_6]^{4-}$ under the (110) and (111) facets.

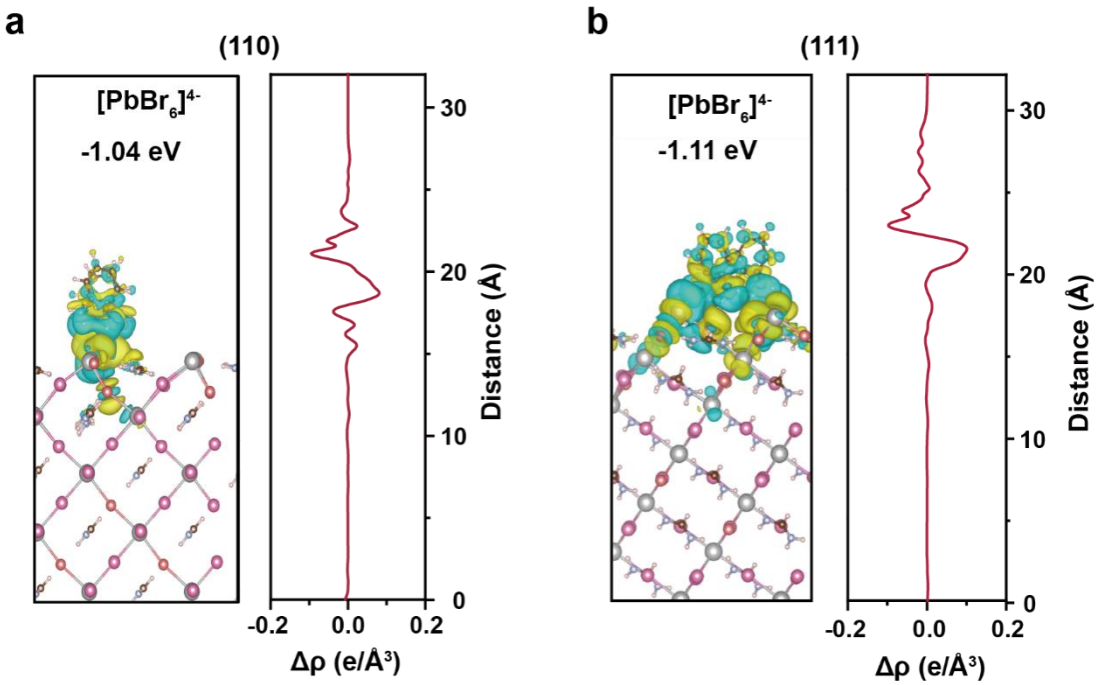

Supplementary Fig. 7 | The binding energy and longitudinal integral curves of differential charge density between OPD and the $[PbBr_6]^{4-}$ at (**a)** (110) and (**b)** (111) facets.

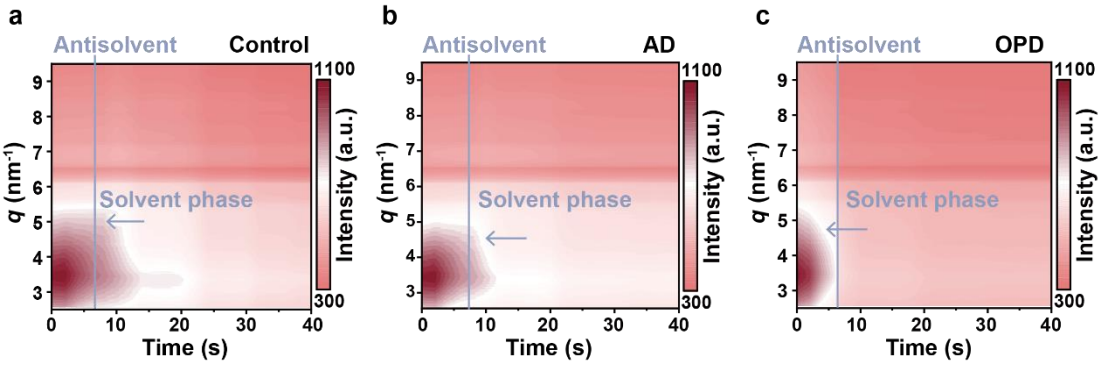

Supplementary Fig. 8 | *In-situ* GIWAXS patterns (2.5 - 9.5 nm^{-1}) of **(a)** control, (**b)** AD-treated, and (**c)** OPD-treated perovskite films at the spin-coating stage.

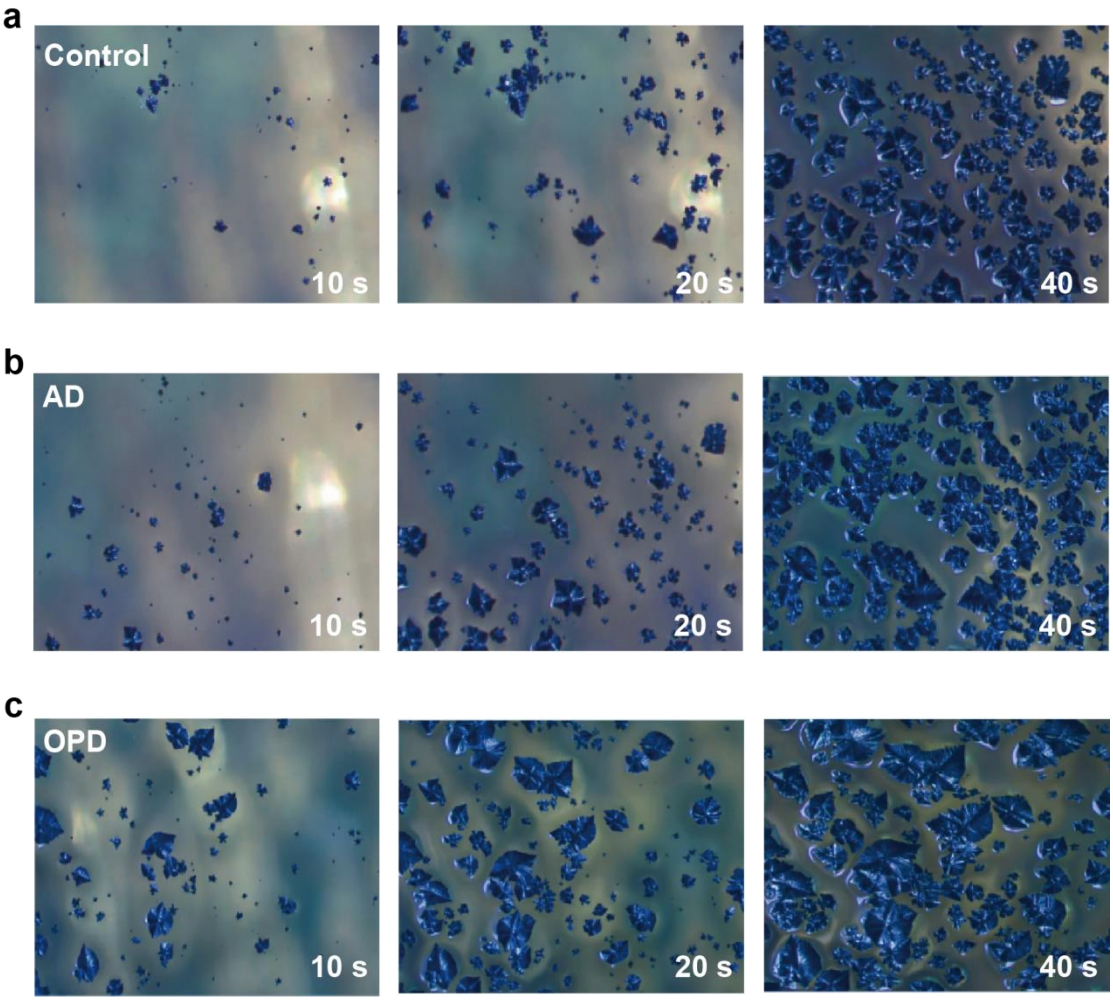

Supplementary Fig. 9 | LSCM images of *in-situ* crystallization kinetics for **(a)** control, **(b)** AD-treated, and **(c)** OPD-treated perovskite precursor solution.

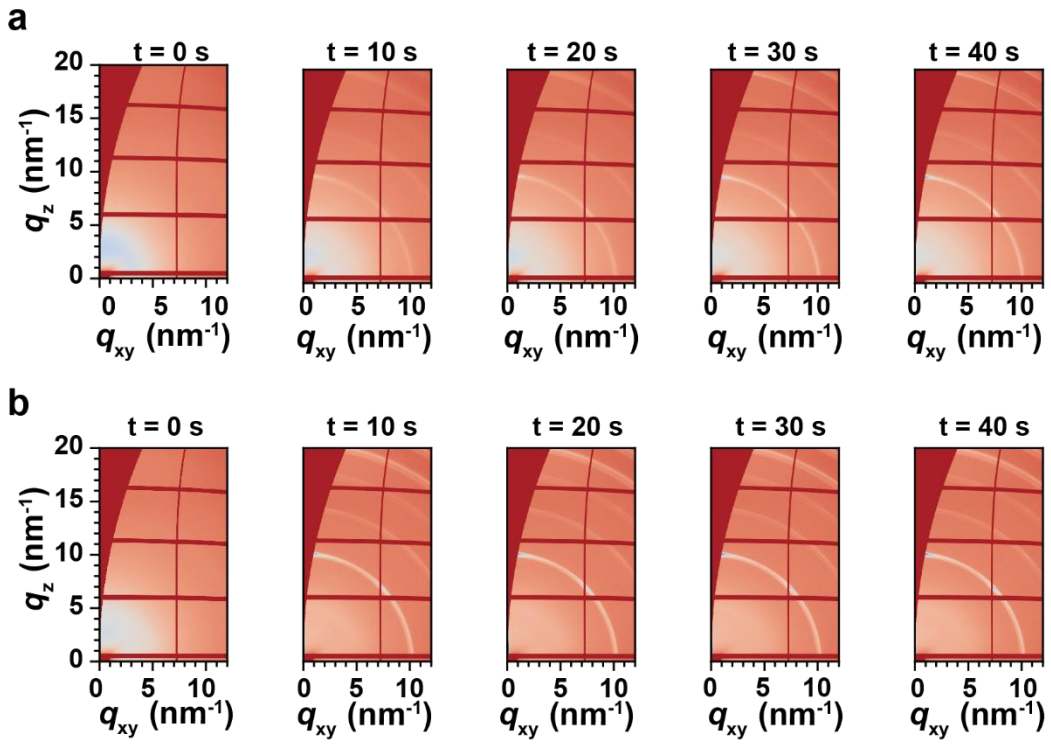

Supplementary Fig. 10 | *In-situ* GIWAXS patterns of (**a)** AD -treated and (**b)** OPD-treated perovskite films.

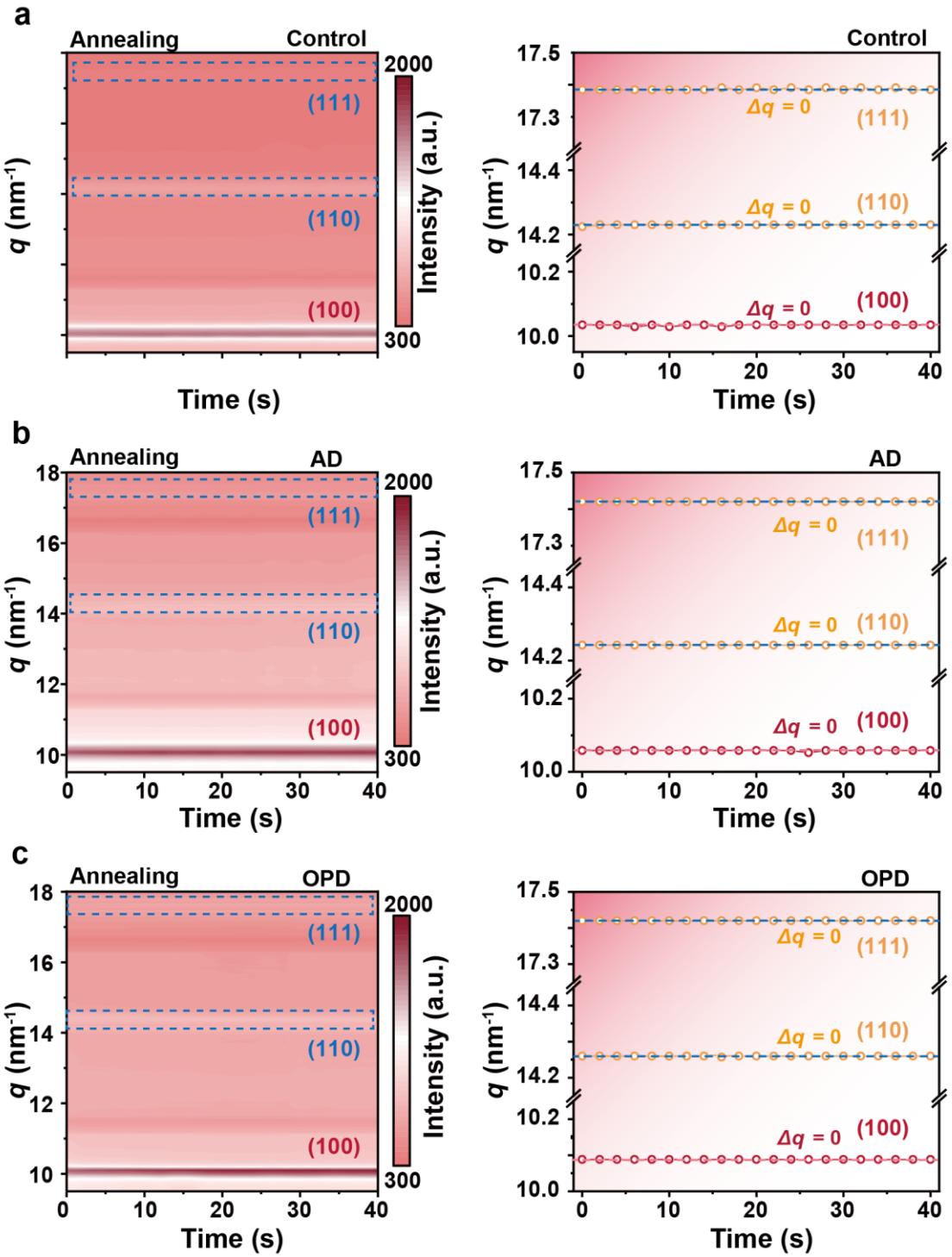

Supplementary Fig. 11 | *In-situ* GIWAXS patterns and extracted *q*-value evolution of (**a**) control, (**b**) AD-treated, and (**c**) OPD-treated films at the annealing growth stage.

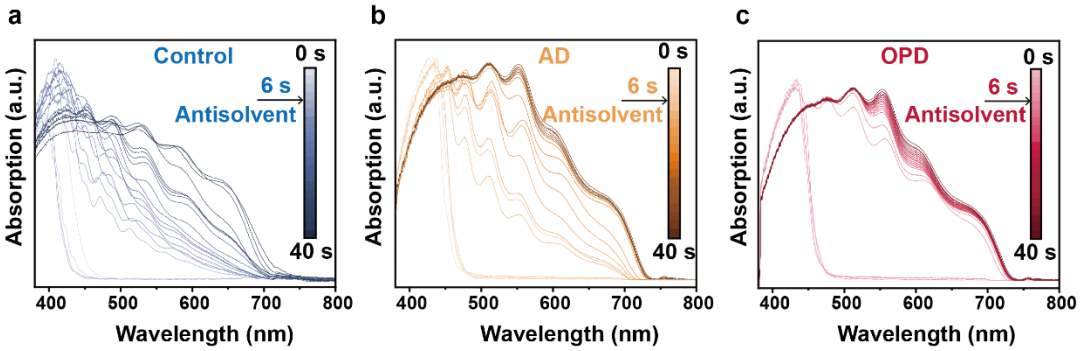

Supplementary Fig. 12 | *In-situ* UV-Vis absorption spectra of (**a)** control, (**b)** AD-treated, and (**c)** OPD-treated perovskite films at the spin-coating stage.

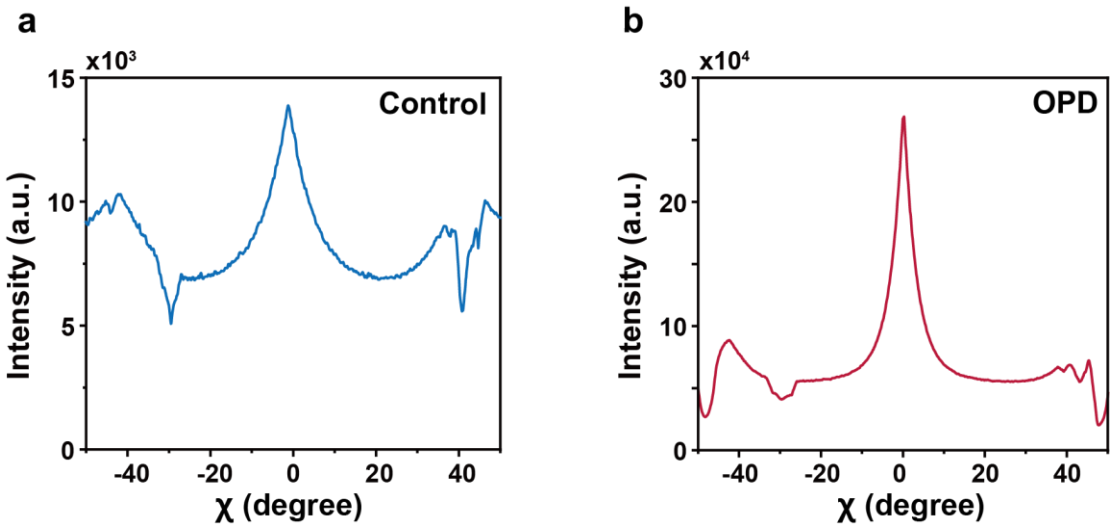

Supplementary Fig. 13 | Extracted the GIWAXS signal intensity of (**a)** control and (**b)** OPD-treated perovskite films.

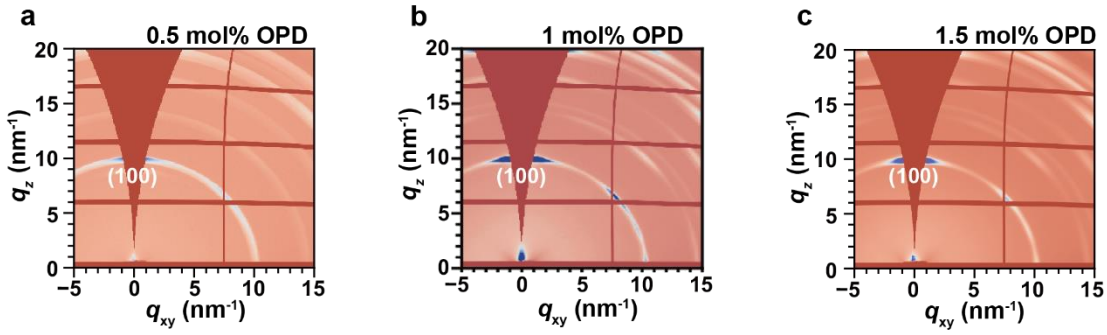

Supplementary Fig. 14 | GIWAXS patterns of perovskite films with (**a)** 0.5 mol%, (**b)** 1 mol%, and (**c)** 1.5 mol% OPD.

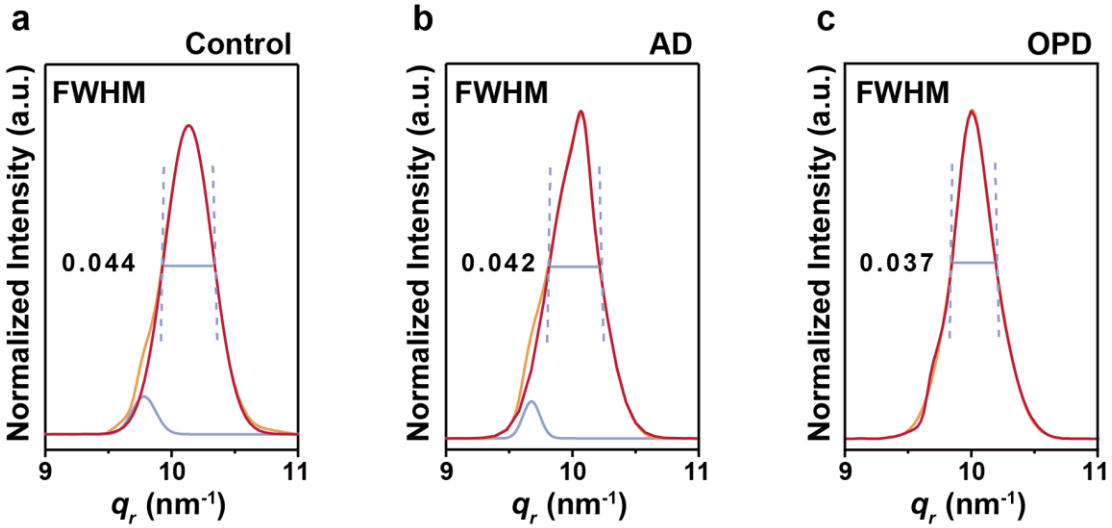

Supplementary Fig. 15 | Full Width at Half Maximum of (100) facet extracted from GIWAXS for (**a)** control, (**b)** AD-treated, and (**c)** OPD-treated perovskite films.

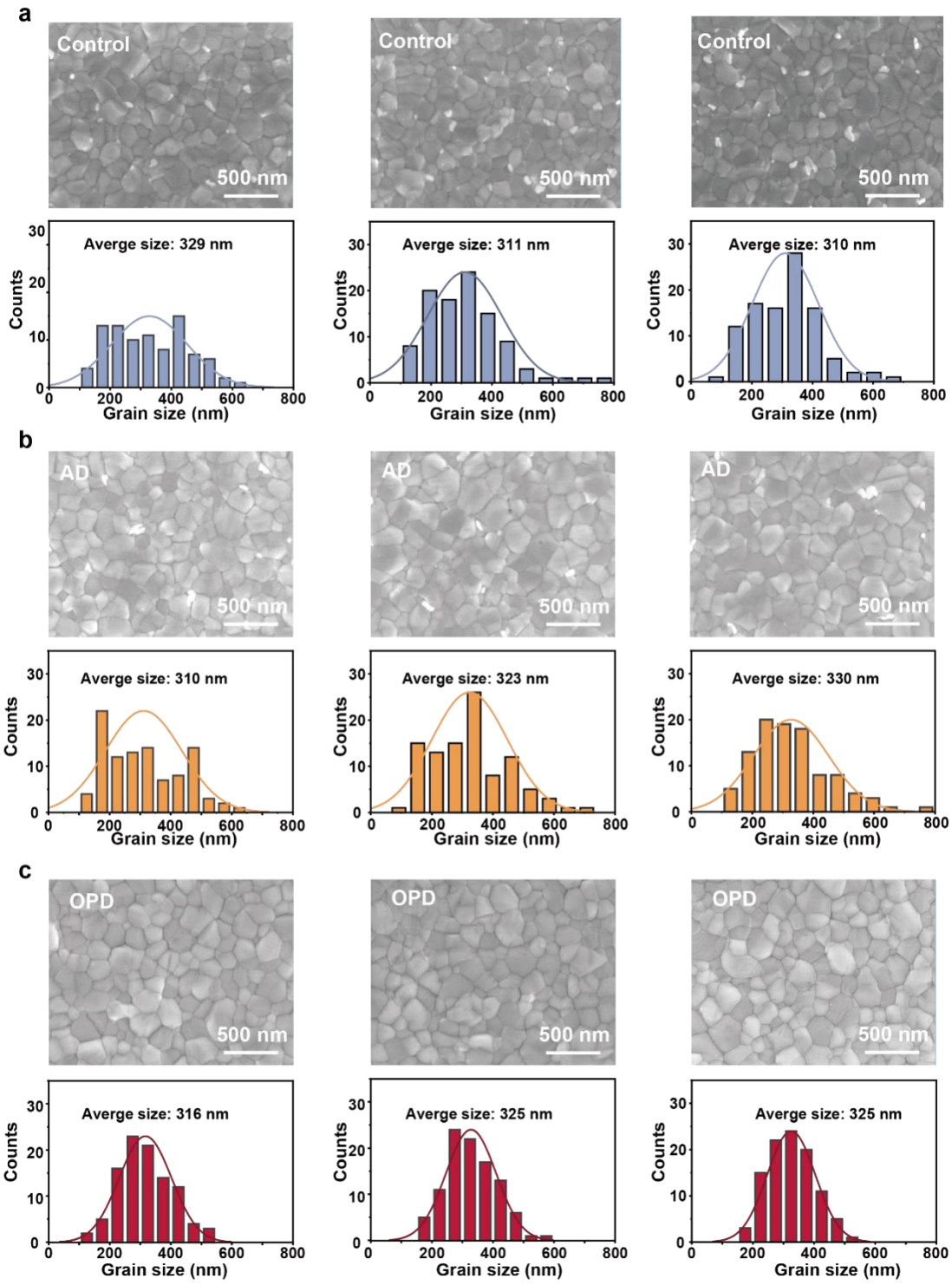

Supplementary Fig. 16 | SEM images and grain size statistics for (**a)** control, (**b)** AD-treated, and (**c)** OPD-treated of perovskite films.

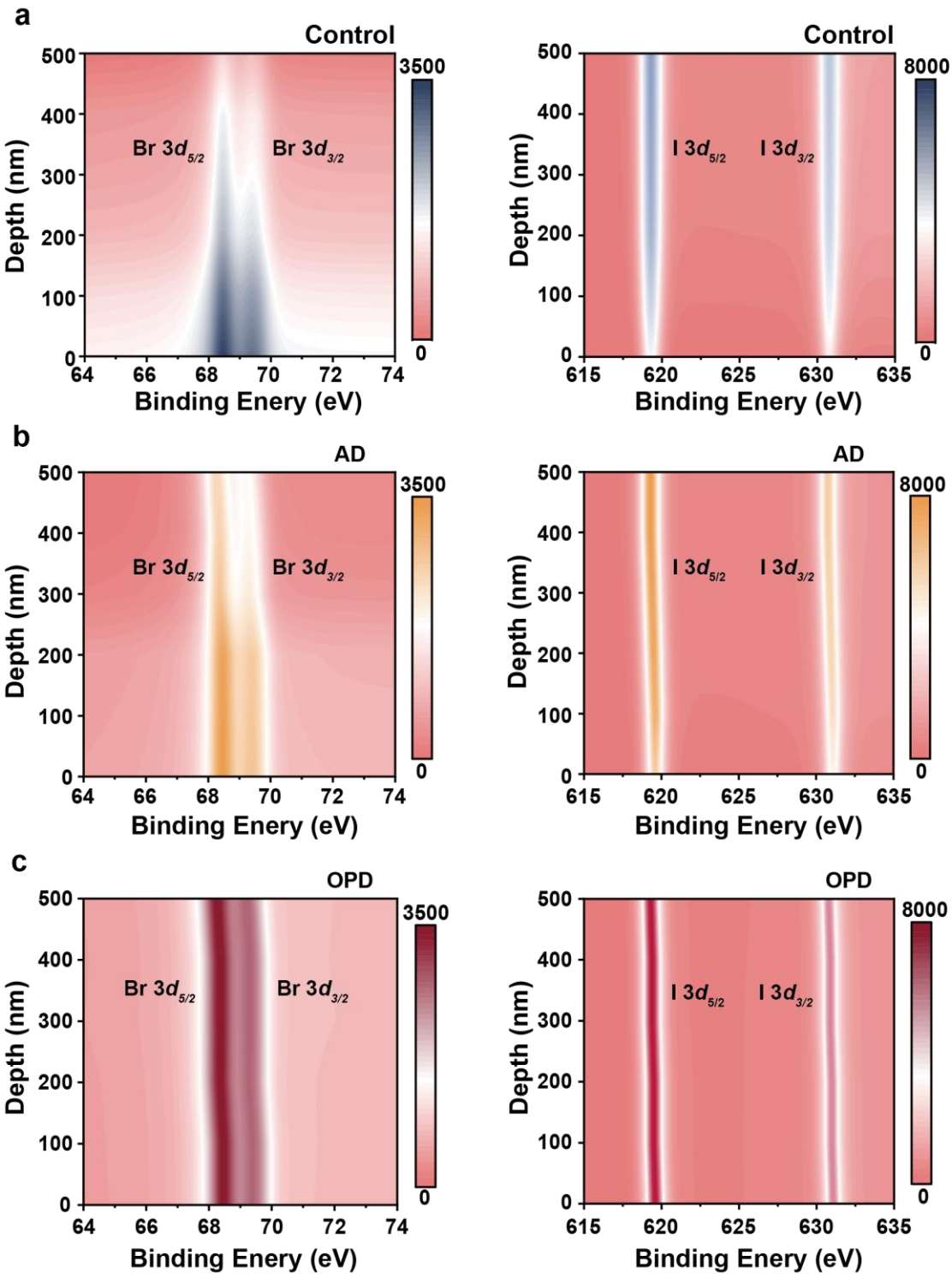

Supplementary Fig. 17 | Depth-profiling XPS spectra of Br and I elements of (**a**) control, (**b**) AD-treated, and (**c**) OPD-treated perovskite films.

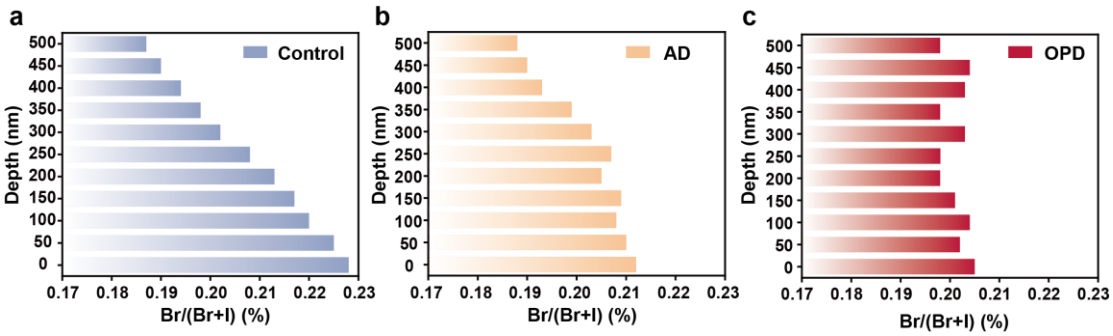

Supplementary Fig. 18 | Halogen distribution statistics extracted from cross-sectional EDS spectra at different depths of (**a**) control, (**b**) AD-treated, and (**c**) OPD-treated samples.

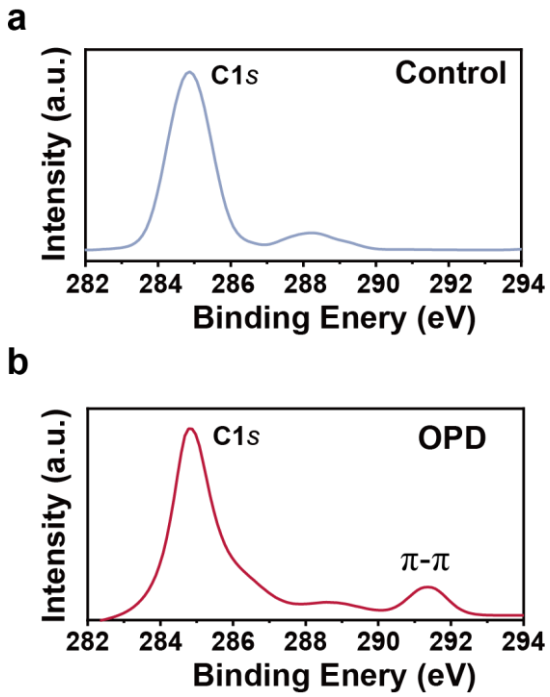

Supplementary Fig. 19 | C 1*s* XPS spectra of (**a)** control and (**b)** OPD-treated perovskite films.

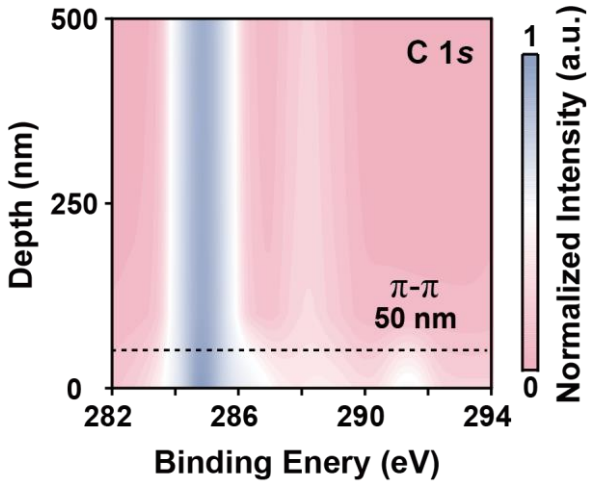

Supplementary Fig. 20 | Depth-profiling XPS spectra of C 1*s* of OPD-treated perovskite film.

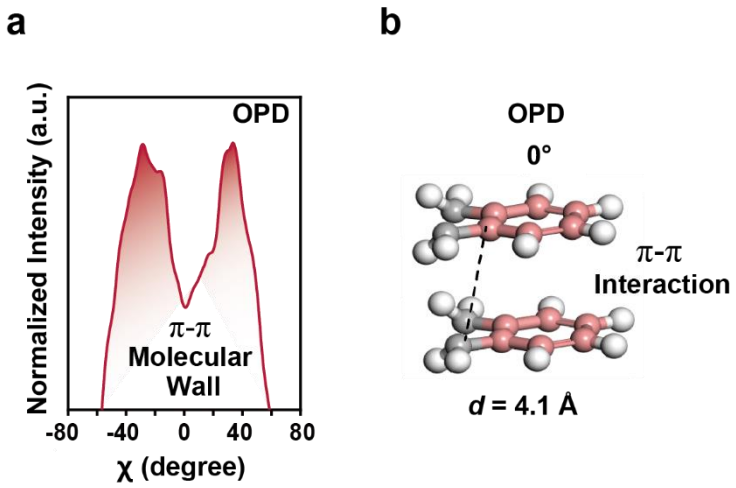

Supplementary Fig. 21 | a Integration of angle and intensity in the anisotropic GIWAXS pattern. **b** Interplanar spacing of OPD molecules with parallel stacking by DFT simulation calculations.

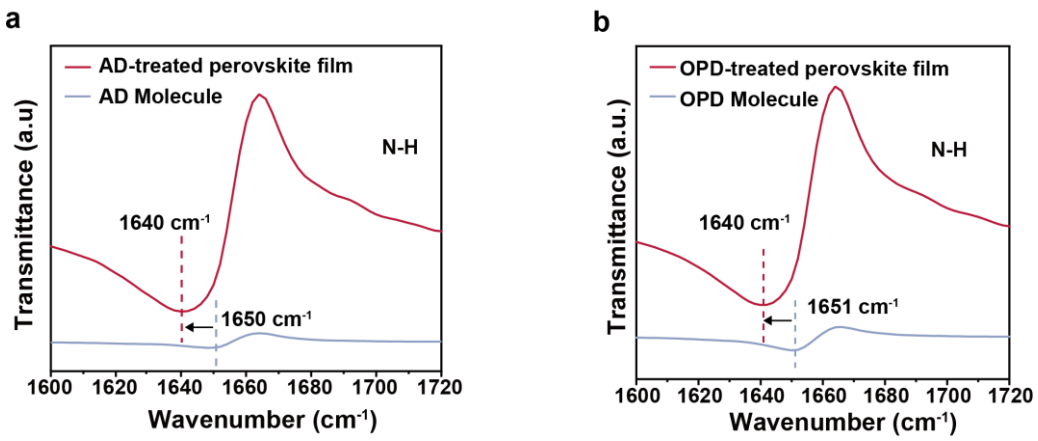

Supplementary Fig. 22 | FTIR for **(a)** AD-treated and **(b)** OPD-treated perovskite films.

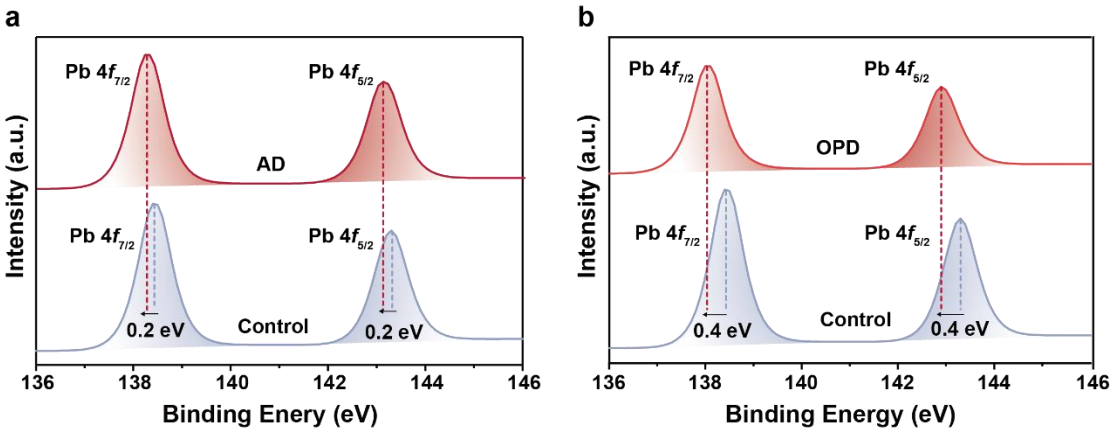

Supplementary Fig. 23| The XPS spectra of Pb 4*f* for (**a)** AD-treated and (**b)** OPD-treated perovskite films.

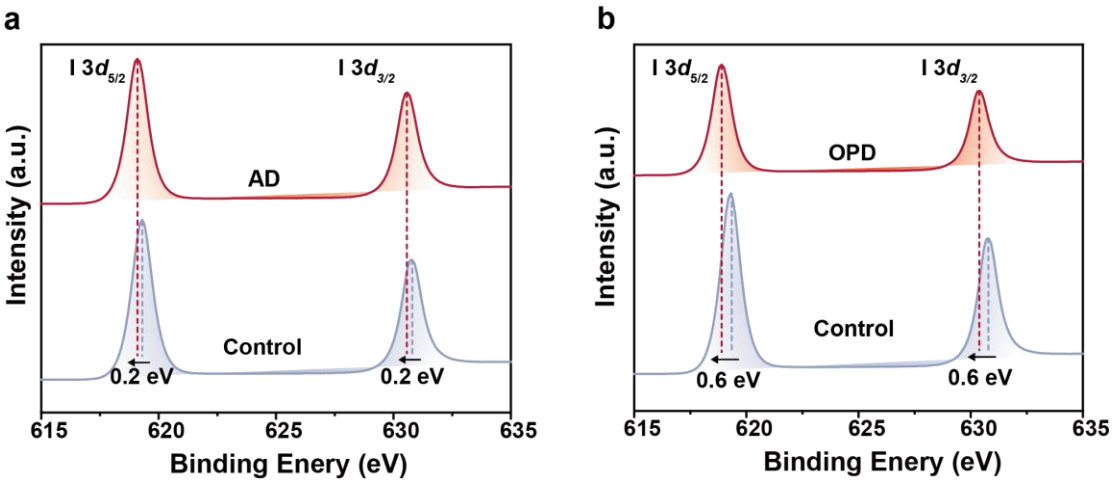

Supplementary Fig. 24 | The XPS spectra of I 3*d* for (**a)** AD-treated and (**b)** OPD-treated perovskite films.

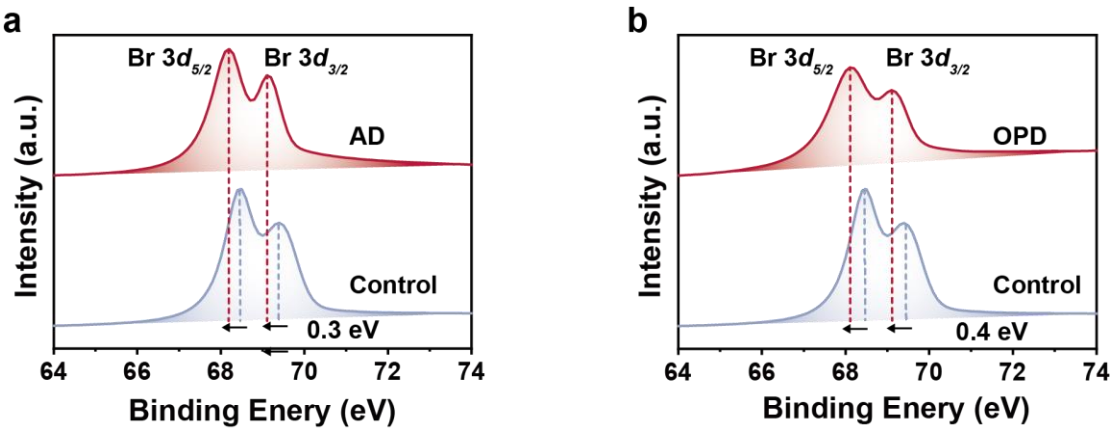

Supplementary Fig. 25 | The XPS spectra of Br 3*d* for (**a)** AD-treated and (**b)** OPD-treated perovskite films.

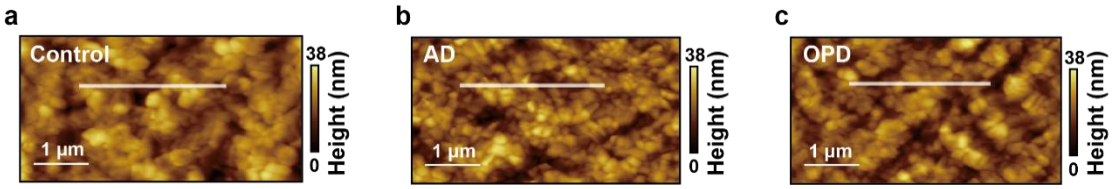

Supplementary Fig. 26 | KPFM topography images for **(a)** control, **(b)** AD-treated, and **(c)** OPD-treated of perovskite films.

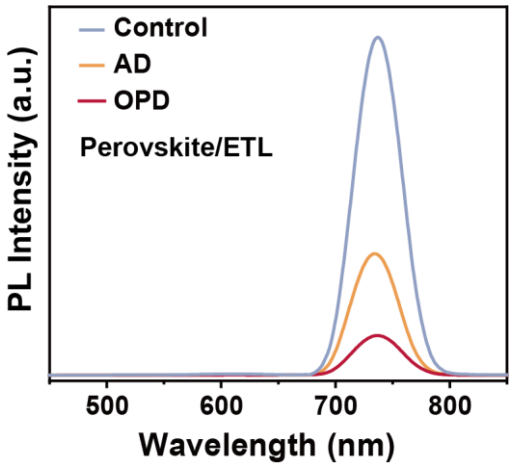

Supplementary Fig. 27 | PL spectra of control, AD-treated, and OPD-treated perovskite/ETL films.

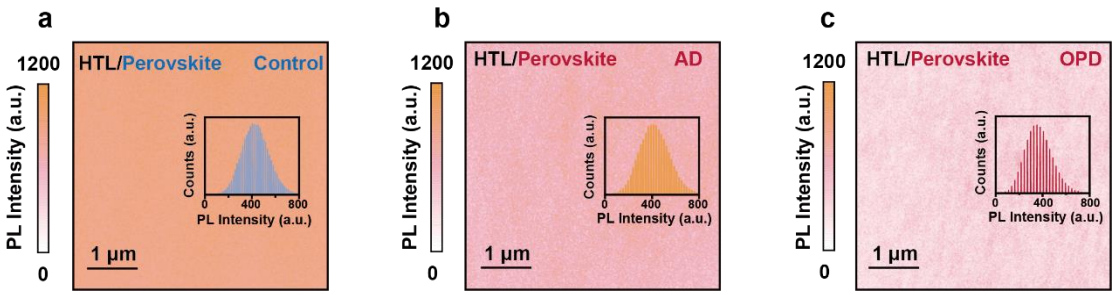

Supplementary Fig. 28 | PL intensity mapping of (**a**) control, (**b**) AD-treated, and (**c**) OPD-treated of perovskite films with HTL.

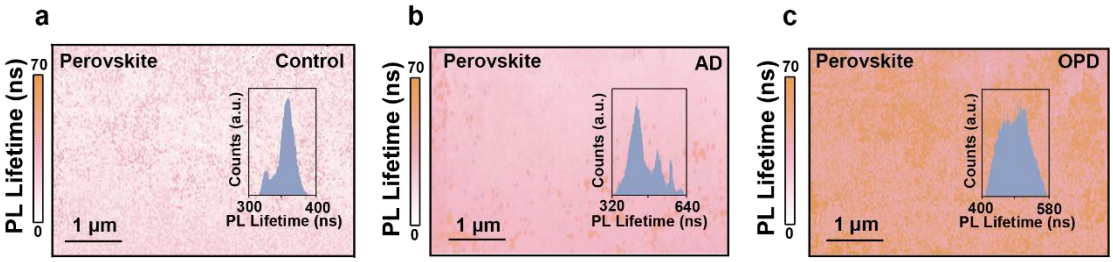

Supplementary Fig. 29 | PL lifetime mappings for **a** control, **b** AD-treated, and **c** OPD-treated perovskite film.

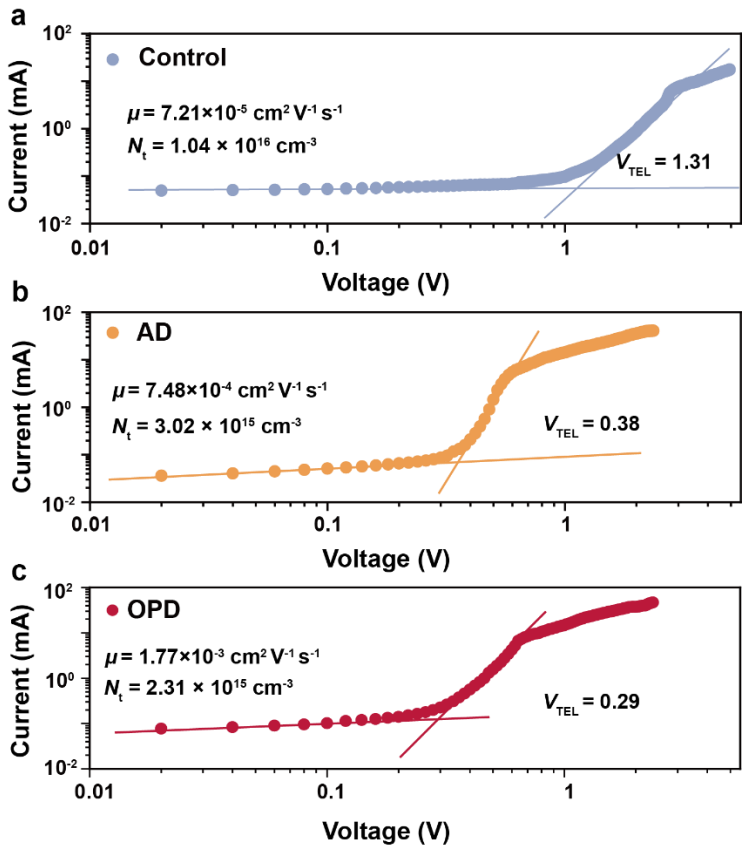

Supplementary Fig. 30 | SCLC curves for (**a**) control, (**b**) AD-treated, and (**c**) OPD-treated perovskite film.

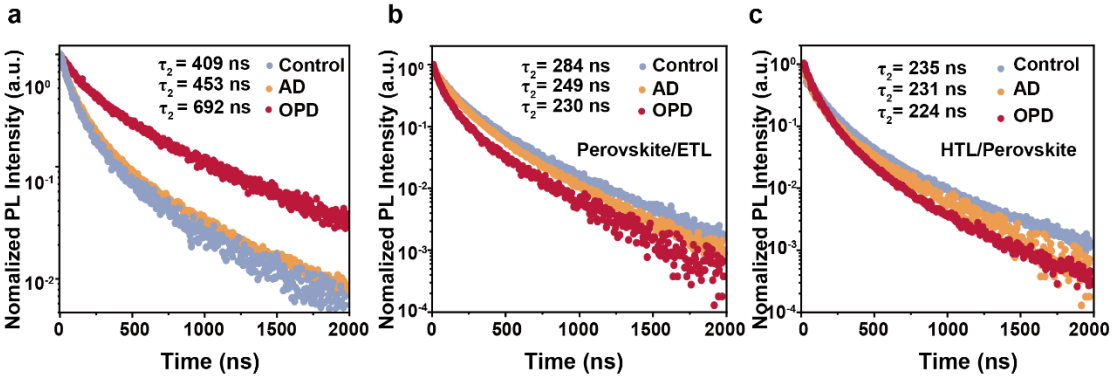

Supplementary Fig. 31 | TRPL decay of (**a)** bare perovskite films, (**b)** perovskite/ETL films, and (**c)** HTL/perovskite films.

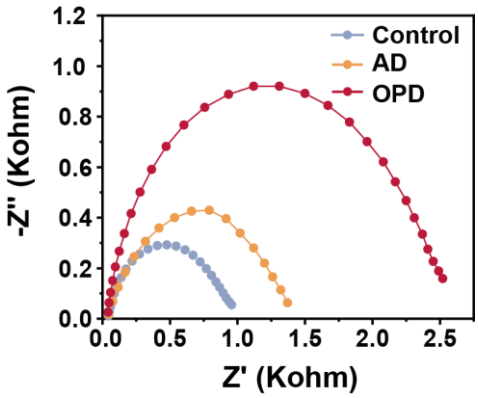

Supplementary Fig. 32 | The EIS spectra of control, AD-treated, and OPD-treated PSCs.

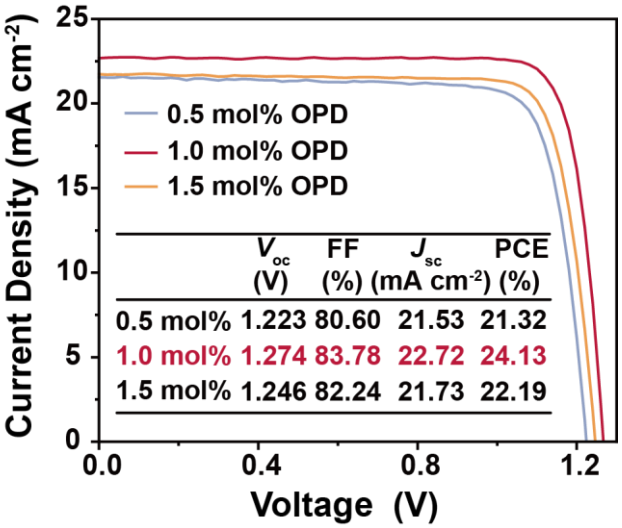

Supplementary Fig. 33 | *J-V* curves of PSCs at different OPD concentrations.

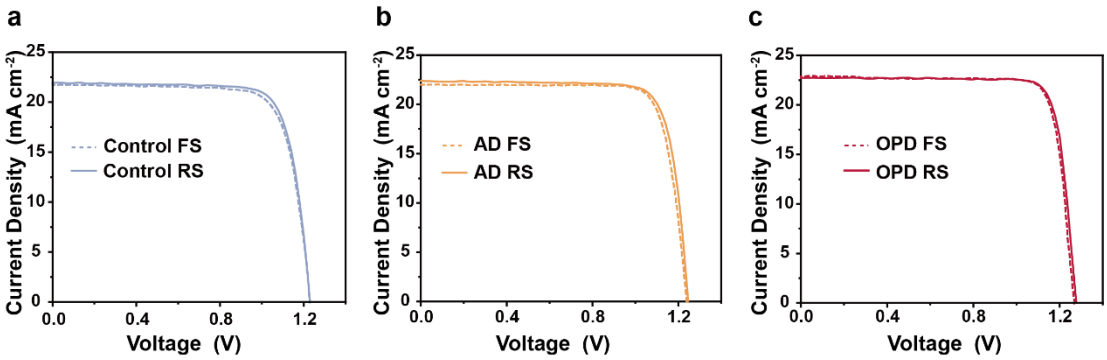

Supplementary Fig. 34 | *J-V* curves with forward and reverse scanning of (**a)** control, (**b)** AD-treated, and (**c)** OPD-treated PSCs.

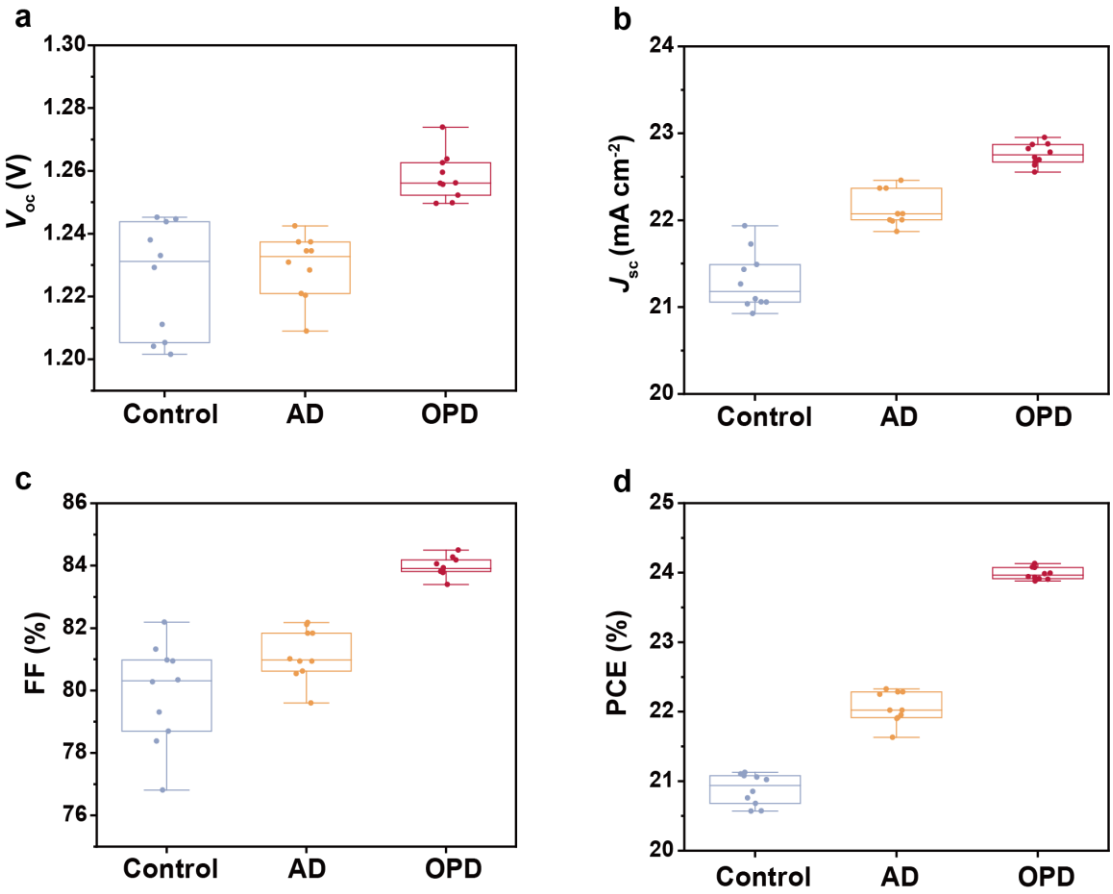

Supplementary Fig. 35 | (a) V_{OC}, **(b)** J_{SC}, **(c)** FF, and **(d)** PCE distribution of control, AD-treated, and OPD-treated PSCs.

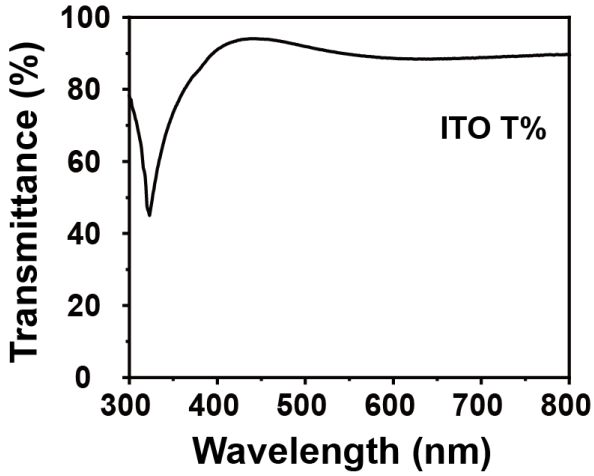

Supplementary Fig. 36 | Transmittance spectrum of glass/ITO.

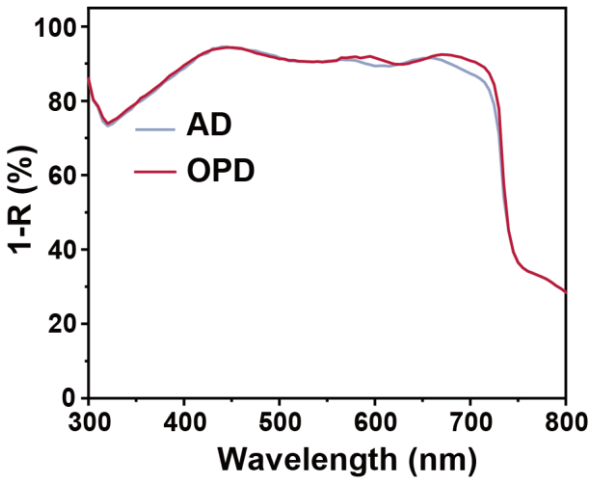

Supplementary Fig. 37 | The 1-R spectra of AD-treated and OPD-treated perovskite films.

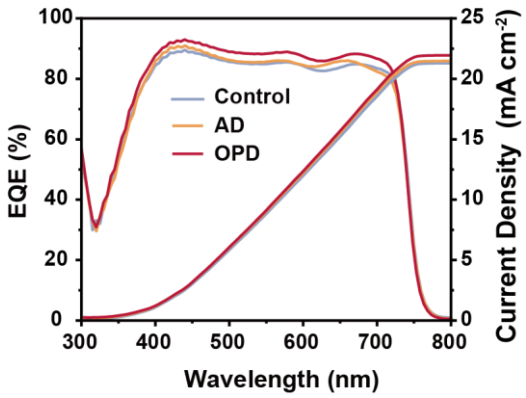

Supplementary Fig. 38 | The EQE spectra of control, AD-treated, and OPD-treated PSCs.

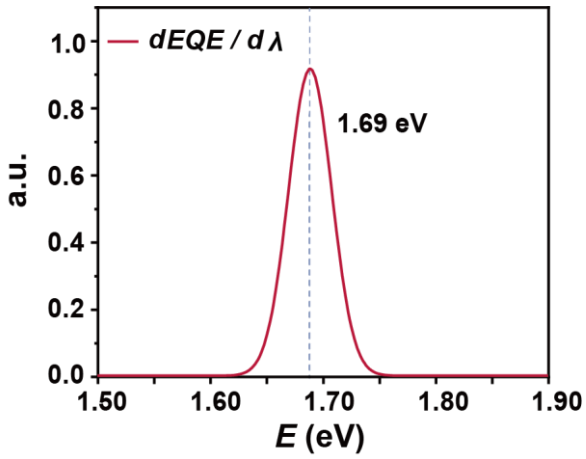

Supplementary Fig. 39 | Bandgap diagram of the device derived from EQE data.

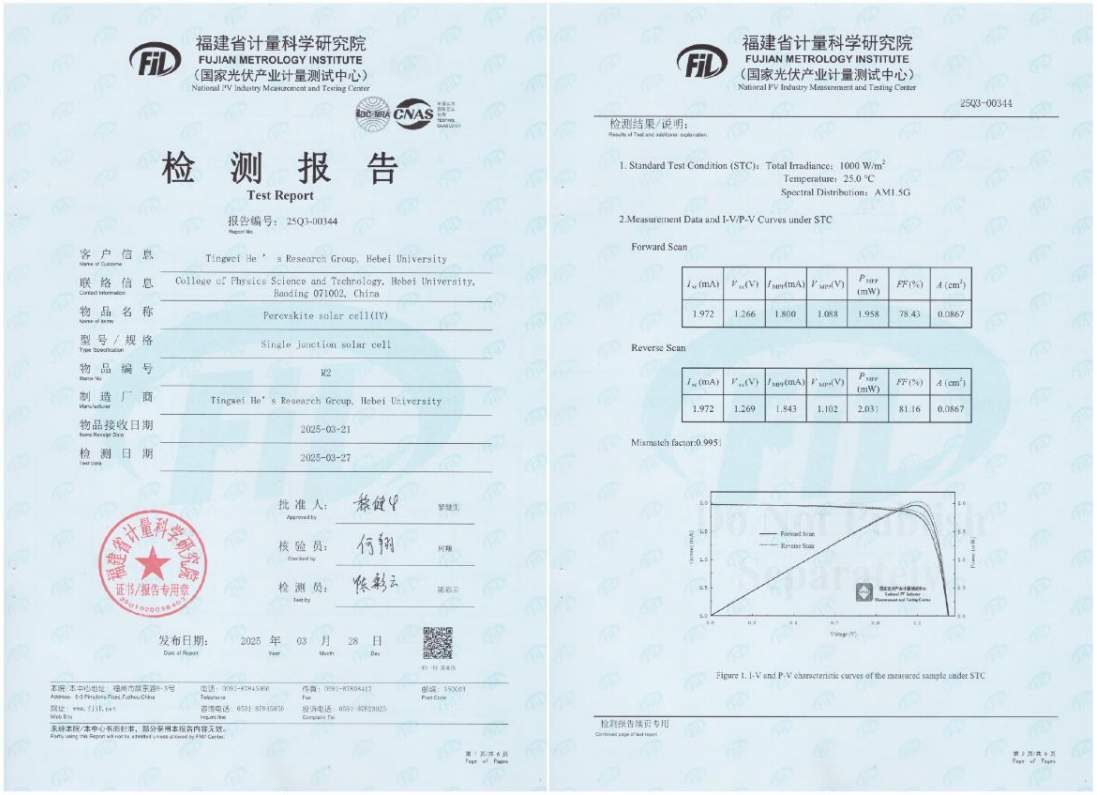

福建省计量科学研究院
FUJIAN METROLOGY INSTITUTE
（国家光伏产业计量测试中心）
National PV Industry Measurement and Testing Center

检 测 报 告
Test Report

报告编号：25Q3-00344

客户信息	Tingwei He ' s Research Group, Hebei University
联络信息	College of Physics Science and Technology, Hebei University, Baoding 071002, China
物品名称	Perovskite solar cell(IV)
型号/规格	Single junction solar cell
物品编号	M2
制造厂商	Tingwei He' s Research Group, Hebei University
物品接收日期	2025-03-21
检测日期	2025-03-27

批准人：
核验员：
检测员：

发布日期：2025 年 03 月 28 日

福建省计量科学研究院
FUJIAN METROLOGY INSTITUTE
（国家光伏产业计量测试中心）
National PV Industry Measurement and Testing Center

25Q3-00344

检测结果/说明：

1. Standard Test Condition (STC): Total Irradiance: 1000 W/m²
Temperature: 25.0 °C
Spectral Distribution: AM1.5G

2.Measurement Data and I-V/P-V Curves under STC

Forward Scan

I_{sc}(mA)	V_{oc}(V)	I_{MPP}(mA)	V_{MPP}(V)	P_{MPP} (mW)	FF(%)	A (cm²)
1.972	1.266	1.800	1.088	1.958	78.43	0.0867

Reverse Scan

I_{sc}(mA)	V_{oc}(V)	I_{MPP}(mA)	V_{MPP}(V)	P_{MPP} (mW)	FF(%)	A (cm²)
1.972	1.269	1.843	1.102	2.031	81.16	0.0867

Mismatch factor:0.995

Figure 1. I-V and P-V characteristic curves of the measured sample under STC

Supplementary Fig. 40 | The third-party certificated performance of OPD-treated PSC at Fujian Institute of Metrology and Science.

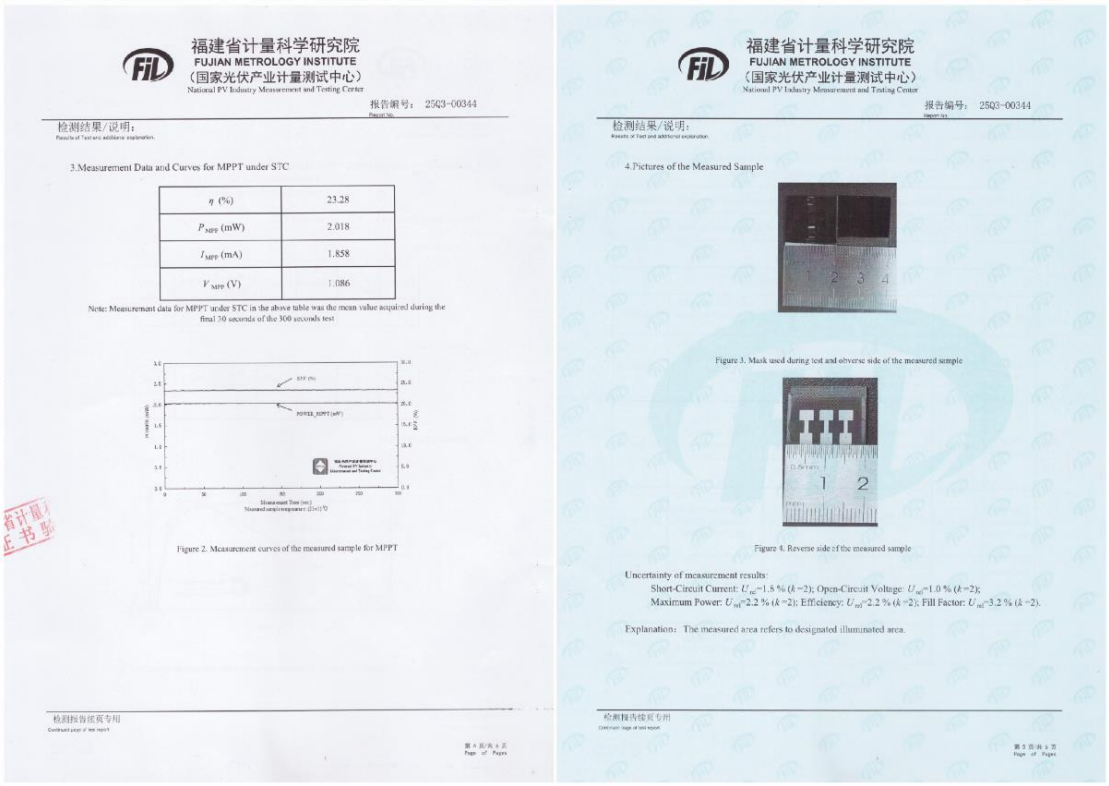

Supplementary Fig. 41 | The third-party certificated MPPT of OPD-treated PSC and mask area of measured sample at Fujian Institute of Metrology and Science.

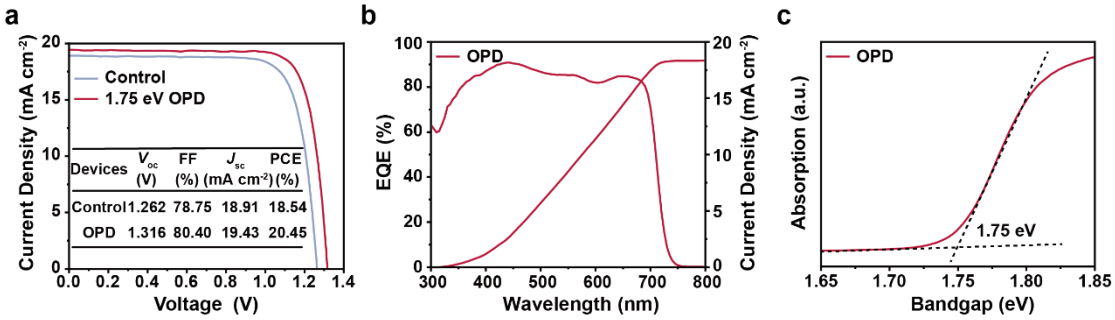

Supplementary Fig. 42 | (a) *J-V* curves and **(b)** EQE spectrum of PSC with Br content of 30 mol%. **c** Absorption spectrum of corresponding perovskite films.

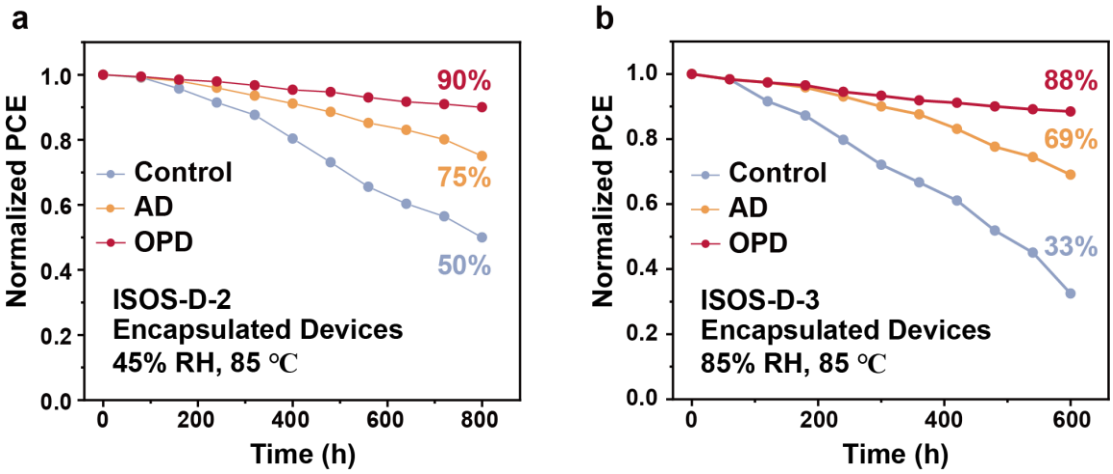

Supplementary Fig. 43 | Damp-heat stability of PSCs under of (**a)** ISOS-D-2 and (**b)** ISOS-D-3 standard protocols.

Supplementary Tables

Supplementary Table S1 | Extracted *q*-value evolution of (100), (110), and (111) facets of control perovskite film at the spin-coating stage.

Time (s)	(100) facet (nm^{-1})	(110) facet (nm^{-1})	(111) facet (nm^{-1})
8	10.148	14.272	17.438
10	10.154	14.272	17.432
12	10.148	14.242	17.426
14	10.130	14.230	17.426
16	10.130	14.224	17.420
18	10.094	14.224	17.403
20	10.058	14.224	17.408
22	10.052	14.230	17.408
24	10.046	14.236	17.402
26	10.035	14.242	17.385
28	10.035	14.224	17.385
30	10.035	14.224	17.391
32	10.035	14.248	17.385
34	10.035	14.230	17.385
36	10.035	14.230	17.391
38	10.035	14.254	17.385
40	10.035	14.248	17.385

Supplementary Table 2. Material parameters used for simulation in SCAPS-1D.

Parameter	ITO	NiO_x	PVK	C_{60}	BCP
Thickness: nm	100	30	500	30	8
Bandgap: eV	3.5	3.4	1.69	2.2	3.5
χ: eV	4.0	3.9	3.9	3.2	3.7
ε	9.0	9.0	18	7	10
N_C: cm^{-3}	2.2×10^{18}	1×10^{21}	2.1×10^{18}	2.2×10^{18}	2.2×10^{18}
N_V: cm^{-3}	1.8×10^{19}	2×10^{20}	2.1×10^{18}	1.8×10^{19}	1.8×10^{19}
μ_e: $cm^{-2}\ V^{-1}\ s^{-1}$	20	20	1.77×10^{-3}	200	200
μ_h: $cm^{-2}\ V^{-1}\ s^{-1}$	10	10	1×10^{-4}	80	80
N_D: cm^{-3}	2×10^{19}	1×10^{19}	-	-	-
N_A: cm^{-3}	-	-	1.0×10^{15}	1.0×10^{18}	1.0×10^{18}
N_t: cm^{-3}	1×10^{15}	1×10^{15}	2.31×10^{15}	1×10^{14}	1×10^{14}
V_e: cm s^{-1}	1.0×10^{7}	1.0×10^{7}	1.0×10^{7}	1.0×10^{7}	1.0×10^{7}
V_h: cm s^{-1}	1.0×10^{7}	1.0×10^{7}	1.0×10^{7}	1.0×10^{7}	1.0×10^{7}

χ: Electron affinities;

ε: Relative dielectric constant;

N_C: Effective state density of conduction band;

N_V: Effective state density of valence band;

μ_e: Electronic mobility;

μ_h: Hole mobility;

N_D: Donor concentration;

N_A: Acceptor concentration;

N_t: Recombination center concentration;

V_e: Thermal velocity of electron;

V_h: Thermal velocity of hole;

Supplementary Table 3. Summary on the photovoltaic parameters of WBG (1.65-1.71eV) PSCs extracted from recent literature.

Ref	E_g (eV)	V_{OC} (V)	J_{SC} (mA cm^{-2})	FF (%)	PCE (%)
1	1.65	1.24	21.4	84.7	22.5
2	1.65	1.26	21.6	82.3	22.5
3	1.65	1.27	-	-	22.7
4	1.65	1.28	21.8	83.8	23.3
5	1.66	1.36	20.44	75.51	21.07
6	1.66	1.23	22.41	82	22.6
7	1.66	1.3	22.38	84.12	24.53
8	1.66	-	-	-	22.53
9	1.66	1.27	22.53	84.33	24.12
10	1.66	1.296	22.02	84.79	24.2
11	1.67	1.29	22.32	85	24.48
12	1.67	1.29	20.4	82.3	21.4
13	1.67	1.28	19.5	84	20.6
14	1.67	1.243	21.58	82.81	22.22
15	1.67	1.255	20.88	85.5	22.4
16	1.67	1.23	21.36	83.66	22
17	1.67	1.26	21.58	85.3	23.2
18	1.67	1.23	22.37	83.76	23.07
19	1.67	1.273	21.27	83.21	22.53
20	1.67	1.246	21.69	84.92	23.05
21	1.67	1.28	-	-	23.25
22	1.67	1.249	21.62	83.98	22.68
23	1.68	1.286	21.42	85.29	23.5
24	1.68	1.24	21.8	84.3	22.8
25	1.68	1.267	21.52	85.1	23.2

26	1.68	1.23	20.8	84.12	21.58
27	1.68	1.286	21.13	83.89	22.8
28	1.68	1.23	21.6	82.85	21.96
29	1.68	1.236	21.12	86.67	22.63
30	1.68	1.23	21.29	84.81	22.12
31	1.68	-	-	-	23.66
32	1.68	1.247	21.11	84.36	22.21
33	1.68	1.251	21.62	83.45	22.57
34	1.68	1.25	22.31	83	23.05
35	1.68	1.268	21.7	82.67	22.76
36	1.68	1.238	21.27	86.7	22.83
37	1.68	1.275	21.68	84.83	23.45
38	1.68	1.3	22.4	80.2	23.4
39	1.68	1.277	21.37	84.08	22.95
40	1.68	-	-	-	22.92
41	1.68	-	-	-	22.35
42	1.68	1.28	-	-	21.5
43	1.69	1.282	22.43	81.2	23.35
44	1.70	1.16	-	-	20.25
45	1.71	1.23	21.97	82.88	21.56
This Work	**1.69**	**1.274**	**22.72**	**83.78**	**24.13**

Supplementary Table 4. The photovoltaic parameters of a 4T TSCs.

Device	V_{OC} (V)	J_{SC} (mA cm^{-2})	FF (%)	PCE (%)
ST-WBG PSCs	1.23	21.98	82.40	22.28
CIGS PSCs	0.76	28.62	80.45	17.49
Filtered CIGS PSCs	0.73	12.91	74.66	7.06
4T tandem cell				29.34

Supplementary Methods

Characterisation of perovskite films

X-ray photoelectron spectroscopy (XPS). Tests were transferred to an ultrahigh vacuum chamber (ESCALAB 250Xi), with a base pressure of 2×10^{-10} mbar, for XPS depth profiling measurements. The depth-profiling XPS measurements were performed using adouble-differentially pumped He gas discharge lamp emitting He I radiation (hν = 21.22 eV).

The Fourier transform infrared spectroscopy (FTIR). Tests were measured on a PerkinElmer Spectrum Two infrared spectrometer.

Kelvin probe force microscopy (KPFM) and atomic force microscopy (AFM, MFP-3D, OXFORD, UK). Tests were performed using a Bruker Dimension Icon system. We used a platinum-iridium-coated PPP-EFM probe to perform measurements in tapping mode. In KPFM mode, an electrical resolution of approximately 10 mV was achieved by setting a phase-locked amplifier and signal filter. The conductive substrate of the perovskite sample was connected to the sample stage. The scanning rate was set to 0.4 Hz to ensure image quality. During the measurement, an AC bias voltage was applied to the probe, and the sample was grounded. Additionally, the AC bias generated an electric field force on the microcantilever that is proportional to the potential difference between the conductive atomic force microscopy probe and the sample.

Scanning electron microscopy (SEM) and energy dispersive X-ray spectroscopy (EDS). Images of perovskite films were characterized using a field emission Scanning Electron Microscope (SEM; JSM-7500F, JEOL).

Photoluminescence (PL) spectra. The steady-state PL spectra were measured by fluorescence spectrophotometer (Edinburgh instruments FLS 980) provided by a xenon lamp, and perovskite films were excited at 435 nm. The excitation source was a laser

diode (450 nm). The excitation source for Time-resolved photoluminescence (TRPL) spectra was a laser diode (450 nm). The photoluminescence lifetime can be defined by a double exponential decay equation:

$$f(t) = A_1 e^{\frac{-t}{\tau_1}} + A_2 e^{\frac{-t}{\tau_2}} \quad (1)$$

The space-charge-limited current (SCLC) measurement. Trap densities and mobilities of FTO/SnO_2/perovskite/PCBM/Ag electron-only device structures were measured using the SCLC model. The dark current-voltage (*I-V*) characteristics of the electron-only devices were measured by a Keithley 2400 source polarimeter. The onset voltage V_{TFL} is linearly related to the defect state density.

$$N_t = \frac{2\varepsilon_0 \varepsilon_r V_{TFL}}{qL^2} \quad (2)$$

$$\mu = \frac{8JL^3}{9\varepsilon_0 \varepsilon_r V_{TEL}^2} \quad (3)$$

Where I is the device current; ε_r is the relative dielectric constant; ε_0 is the vacuum permittivity; q is the elementary charge; L is the perovskite film thickness; J is current density.

Thermal admittance spectroscopy (TAS). The capacitance-frequency curve was measured with a PARSTAT 4000. The energy distribution of the trapped state density can be fitted by the following equation:

$$N_t(E_\omega) = -\frac{V_{bi}}{eW}\frac{dc}{d\omega}\frac{\omega}{k_B T} \quad (4)$$

Where V_{bi} is the built in voltage; ω is angular frequency; e is the elementary charge; W is the depletion width; C is the capacitance; k_B is the Boltzmann constant and T is the temperature.

***In-situ* UV-Vis absorption spectra, transmittance spectra and reflectance spectra.** It was acquired using a UV/vis spectrophotometer (Shimadzu UV-2550) equipped with an integrating sphere. The baseline spectrum (without sample) is acquired before measuring the transmittance of the devices in order to discard the fluctuations of the

lamp installed in our spectrophotometer. Each transmittance spectra is then normalized with respect to the baseline spectrum following this equation:

$$T(\lambda) = \frac{100T_{device}(\lambda)}{T_{baseline}(\lambda)} \quad (5)$$

$$R(\lambda) = (\frac{\vec{n}(\lambda)-n_0}{\vec{n}(\lambda)+n_0})^2 \quad (6)$$

$$\vec{n}(\lambda) = n(\lambda) + ik(\lambda) \quad (7)$$

Where λ is the wavelength, n is the real part of the refractive index, k is the extinction coefficient, n_0 is the refractive index of the incident medium.

Characterization of photovoltaic devices

The Mott-Schottky measurement. Tests were determined the type of semiconductor and the carrier concentration and flat band potential. Space charge layer capacitance and potential *E* could be described by the Mott-Schottky equation. The equation that describes the differential capacitance of the space charge layer in a semiconductor. Mott-Schottky formula:

$$\frac{1}{c^2} = \frac{2}{\varepsilon\varepsilon_0 e N_D}(V - V_{fb} - \frac{k_B T}{e}) \quad (8)$$

In the equation, V_{fb} is the flat band potential; N_D is carrier concentrations; ε is the relative dielectric constant; ε_0 is the vacuum permittivity; k_B is the Boltzmann Constant; T is the absolute temperature; e is the electric quantity per unit charge.

Electrochemical impedance spectra (EIS). Tests were measured using an electrochemical workstation. The light source was simulated by a xenon lamp-based solar simulator and the illumination intensity was adjusted by a filter. Impedance spectra were recorded in the frequency range of 0.2 to 2000 kHz by an Agilent E4980A precision LCR meter and homemade software. For complex resistance (R_{rec}) measurements, a bias voltage equal to V_{oc} was applied to the device under dark conditions.

Electroluminescence quantum efficiency (EQE_{EL}). The test was conducted using the Newport QE measurement kit, which consisted of a xenon lamp, monochromator, chopper and lock-in amplifier, and was equipped with a calibrated silicon photodetector. For the characteristic analysis of light-emitting diode devices, optical output measurements were carried out using a fiber optic integrating sphere (FOIS-1-FL) coupled with a QE 65 Pro spectrometer. The device was measured from zero bias voltage to forward bias voltage, with a scanning rate of 0.1 V s^{-1} and a residence time of 1 s. The characteristics of the device were analyzed using a fiber optic integrating sphere coupled with the QE 65 Pro spectrometer.

Theoretical Calculations

Calculation of the distance of facet. All calculations were carried out within the framework of density functional theory, using the project-enhanced facet wave method, which was implemented by the Vienna ab initio simulation package[46]. The commutation-correlation potential function adopts the generalized gradient approximation proposed by Perdew, Burke and Ernzerhof. Long-range van der Waals interactions are described using the DFT-D3 method [47,48]. The energy is truncated by A facet wave of 400 eV, with the energy convergence accuracy set at 1×10^{-5} eV atom^{-1}, and the force acting on each atom does not exceed 0.01 eV/A^{-1}. The Brillouin District is integrated using a 3 × 3 × 1 k-point grid.

Intermolecular interaction. All first-principle density functional theory (DFT) calculations for the Binding energy between cluster models were carried out using the Materials Studio (MS) with projector augmented-wave (PAW) potentials method. Geometry optimization using the generalized gradient approximation (GGA) of the Perdew-Burke-Ernzerhof (PBE) was used for the exchange-correlation functional, since it provides sufficient accuracy at an acceptable computational cost. The weak interaction forces are considered, and the accuracy of the calculation is guaranteed by combining the hybrid DFT model with the Grimme DFT-D3 dispersion correction of Becke-Johnson damping function, which was employed to improve the description of the long-range van der Waals interaction[48]. The energy and force convergence parameters were set at 6^{-10} eV and 0.02 Ha Å^{-1}. 15 Å × 15 Å × 15 Å cell with 1 × 1 × 1 Γ-centered k-point grid was utilized. The adsorption energy between cluster models is defined as follows:

$$\Delta E = E_{AB} - (E_A + E_B) \quad (9)$$

In this equation, E_A, E_B, and E_{AB} are the energies of neutral A, B, and the whole system, respectively.

Binding energy between molecules and facet. All calculations were carried out within

the framework of density functional theory, using the project-enhanced facet wave method, which was implemented by the Vienna ab initio simulation package. The commutation-correlation potential function adopts the generalized gradient approximation proposed by Perdew, Burke and Ernzerhof. Long-range van der Waals interactions are described using the DFT-D3 method[46,47]. The facet wave truncation energy is set at 400 eV, the energy convergence accuracy is set at 1×10^{-5} eV $atom^{-1}$, and the force acting on each atom does not exceed 0.01 eV A^{-1}. In the Brillouin district, a 1×1×1 k-point grid is used to integrate (100) and (110) PVK, and a 2×2×1 k-point grid is used to integrate (111) PVK. The interaction can be calculated by the following equation:

$$E_{int} = E_{(perovskite\ \&\ additive\ molecule)} - E_{perovskite} - E_{additive\ molecule} \quad (10)$$

SCAPS (Solar Cell Capacitance Simulator). The test was a numerical simulation of perovskite solar devices based on the fundamental equations of semiconductor physics and a self-consistent solution framework. The core of SCAPS was solved iteratively by coupling the Poisson equation, the electron-hole continuity equation, and the carrier transport equation with preset one-dimensional device geometries and hierarchical material parameters. The calculations strictly incorporate the characteristic physical models of perovskite materials, including but not limited to: defect state distribution (e.g., single energy level/Gaussian distribution defects in the bandgap), Shockley-Read-Hall composites, radiative composites, Auger composites, interfacial composites, ion mobility effects (via modified migration-diffusion equations or equivalent circuit models), energy band shifts, and tunnelling mechanisms. Boundary conditions were set based on the device electrode contact characteristics, and the carrier generation rate distribution under light conditions is considered. The solver used numerical methods (e.g., Newton's iterative method) to discretize the system of equations on a spatial grid until a convergence criterion was reached, and finally outputs key performance parameters such as steady-state or transient current-voltage characteristics *(J-V* curves), quantum efficiency (QE), capacitance-voltage characteristics (*C-V*), energy band

diagrams, and carrier concentration and complexity distributions of the devices. Solve the Poisson and continuity equations for electrons and holes according to the following equations[49]:

$$\frac{d}{dx}\left[-\varepsilon(x)\frac{d\varphi}{dx}\right] = q[p_h(x) - n_e(x) + N_A^-(x) + p_t(x) - n_t(x)] \quad (11)$$

$$-\frac{1}{q}\frac{\partial J_n}{\partial x} - G(x) + R_n(x) = 0 \quad (12)$$

$$-\frac{1}{q}\frac{\partial J_p}{\partial x} - G(x) + R_p(x) = 0 \quad (13)$$

Where, ε is the relative permittivity; q is the electrical charge; N_A and N_D are the acceptor and donor concentrations, respectively; φ is the electrostatic potential; $G(\chi)$ is the optical generation rate; χ indicates the coordinate position; $P_t(\chi)$ and $P_t(\chi)$ are the trapped holes and electrons, respectively; and ne and P_h indicate electron and hole densities, respectively. J_n and J_p denote the current densities of electrons and holes, respectively, and $R_n(\chi)$ and $R_p(\chi)$ denote the recombination rates of electrons and holes, respectively.

Supplementary References

1. Guo, Y. et al. A universal surface fixed charge reconstruction strategy to minimize contact loss in wide bandgap perovskite photovoltaics. *Energy Environ. Sci.* **10**, 4916-4924 (2025).
2. Liu, Z. et al. Synergistic solvent and composition engineering of perovskites for tandems on industrial silicon. *Angew. Chem. Int. Ed.* **64**, e202424809 (2025).
3. Wang, J. et al. Performance and stability analysis of all-perovskite tandem photovoltaics in light-driven electrochemical water splitting. *Nat. Commun.* **16**, 174 (2025).
4. Yang, G. et al. Reductive cation for scalable wide-bandgap perovskite solar cells in ambient air. *Nat. Sustain.* **8**, 456-463 (2025).
5. Tahir, S. et al. Computational insights into wide bandgap lead free perovskite solar cells for silicon based tandem configurations. *Sci. Rep.* **15**, 20020 (2025).
6. Anand, S. et al. Efficient blade-coated perovskite/silicon tandems via interface engineering. *Joule* **9**, 101767 (2025).
7. Wang, Z. et al. Regulation of wide bandgap perovskite by rubidium thiocyanate for efficient silicon/perovskite tandem solar cells. *Adv. Mater.* **36**, 2407681 (2024).
8. Feng, Z. et al. Buried interface modulation using self-assembled monolayer and ionic liquid hybrids for high-performance perovskite and perovskite/$CuInGaSe_2$ tandem photovoltaics. *Adv. Mater.* **37**, 2407681 (2025).
9. Li, H. et al. Stabilizing grain boundaries by in situ formation of robust layered metallo-organic complex toward high-performance inverted perovskite solar cells. *Adv. Mater.* e11124 (2025).
10. Zhang, Z. et al. Immobilizing lead and healing surface defects via perfluorinated tertiary amine molecules enables high-performance sustainable inverted perovskite solar cells. *Adv. Mater.* 2508126 (2025).
11. Fang, Z. et al. Surface reconstruction of wide-bandgap perovskites enables efficient perovskite/silicon tandem solar cells. *Nat. Commun.* **15**, 10554 (2024).

12. Zheng, L. et al. Strain-induced rubidium incorporation into wide-bandgap perovskites reduces photovoltage loss. *Science* **388**, 88-95 (2025).
13. Lin,Y. et al. Bandgap-universal passivation enables stable perovskite solar cells with low photovoltage loss. *Science* **384**,767-775 (2024).
14. Li, J. et al. Homogenizing the halogen distribution via a multifunctional fluorine-containing additive toward high-performance inverted wide-bandgap perovskite solar cells. *Adv. Funct. Mater.* **35**, 2422175 (2025).
15. Guo, Y. et al. Contact potential homogenization via buried interface engineering enables high-performance wide-bandgap perovskite photovoltaics. *Adv. Funct. Mater.* **35,** 2500168 (2025).
16. Ge, X. et al. Electronic homogenization regulation via nicotinamide derivative ligands for efficient blade-coated wide-bandgap perovskite solar cells. *Adv. Funct. Mater.* 2503504 (2025).
17. Wang, S. et al. Sweet zwitterionic aspartame for high-performance wide-bandgap perovskite solar cells and tandem devices. *Adv. Funct. Mater.* 2503592 (2025).
18. Yang, L. et al. Modulating binding strength and acidity of benzene-derivative ligands enables efficient and hysteresis-free perovskite/silicon tandem solar cells. *Angew. Chem. Int. Ed.* **64**, e202500350 (2025).
19. Guo, C. et al. Bifacially reinforced self-assembled monolayer interfaces for minimized recombination loss and enhanced stability in perovskite/silicon tandem solar cells. *Adv. Mater.* 2504520 (2025).
20. Wu, S. et al. Customized multifunctional additive regulates 1.67 eV-wide-bandgap perovskite crystallization for four-terminal perovskite/silicon tandem solar cells. *Adv. Mater.* 2503269 (2025).
21. Yang, Y. et al. Activating halogen circulation enables efficient and stable wide-bandgap mixed-halide perovskite solar cells. *Adv. Mater.* **37**, 2416513 (2025).
22. Luo, Z. et al. Albendazole passivation in inverted wide-bandgap perovskite solar cells toward efficient perovskite/$CuInGaSe_2$ tandem photovoltaics. *Adv. Mater.* e05597 (2025).

23. Pei, F. et al. Inhibiting defect passivation failure in perovskite for perovskite/ $CuInGaSe_2$ monolithic tandem solar cells with certified efficiency 27.35%. *Nat. Energy* **10**, 824-835 (2025).
24. Luo, Y. et al. Inductive effects in molecular contacts enable wide-bandgap perovskite cells for efficient perovskite/TOPCon tandems. *Nat. Commun.* **16**, 4516 (2025).
25. Tian, L. et al. Divalent cation replacement strategy stabilizes wide-bandgap perovskite for $CuInGaSe_2$ tandem solar cells. *Nat. Photon.* **19**, 479-485 (2025).
26. Pei, F. et al. A binary 2D perovskite passivation for efficient and stable perovskite/ silicon tandem solar cells. *Nat. Commun.* **15**, 7024 (2024).
27. Ye, T. et al. Molecular bridge in wide-bandgap perovskites for efficient and stable perovskite/silicon tandem solar cells. *Adv. Funct. Mater.* **35**, 2419391 (2025).
28. Zhu, Y. et al. Fluorinated pyrimidine bridged buried interface for stable and efficient wide-bandgap perovskite solar cells. *Adv. Funct. Mater.* **35**, 2417310 (2025).
29. Li, C. et al. Enhancing efficiency of industrially-compatible monolithic perovskite/silicon tandem solar cells with dually-mixed self-assembled Monolayers. *Adv. Funct. Mater.* **34**, 2407805 (2024).
30. Liu, Z. et al. Scalable interface engineering in wide-bandgap perovskite solar cells via blade-coating molecules with promoted parallel orientation. *Adv. Funct. Mater.* 2510444 (2025).
31. Cai, Q. et al. Enhancing electron transport for efficiency-recorded HTL-free inverted perovskite solar cells by molecular complementary passivation. *Joule* **9**, 101880 (2025).
32. Shi, B.et al. Halogen anion pre-homogenization of sequentially deposited wide bandgap perovskites for commercial textured perovskite/silicon tandem solar cells. *Energy Environ. Sci.* **18**, 6297-6306 (2025).
33. Zhou, W. et al. A universal strategy for defects and interface management enables highly efficient and stable inverted perovskite solar cells. *Energy Environ. Sci.* **18**, 3828-3838 (2025).

34. Huang, T. et al. Rational heterostructure stacking enables 23% wide-bandgap perovskite solar cells by side-reaction inhibition. *Energy Environ. Sci.* **17**, 5984-5992 (2024).
35. Zhao, H. et al. Synergistic self-Assembled monolayers reinforce buried interface anchoring for high-efficiency tandem perovskite solar cells. *Angew. Chem. Int. Ed.* e202504237 (2025).
36. Li, C. et al. Achieving 32% efficiency in perovskite/silicon tandem solar cells with bidentate-anchored superwetting self-assembled molecular layers. *Angew. Chem. Int. Ed.* e202502730 (2025).
37. Li, Z. et al. Sustainable molecular passivation via heat-induced disaggregation and redox reactions for inverted perovskite solar cells. *ACS. Energy Lett.* **9**, 5471-5482 (2024).
38. Li, Z. et al. Nanocrystal-nucleus template strategy for efficient wide-bandgap perovskite solar cells with enhanced homogeneity and energy-level alignment. *Adv. Mater.* 2509202 (2025).
39. Wang, L. et al. Highly efficient monolithic perovskite/TOPCon silicon tandem solar cells enabled by "Halide Locking". *Adv. Mater.* **37**, 2416150 (2025).
40. Yang, S. et al. Buried interface strategies with covalent organic frameworks for high performance inverted perovskite solar cells. *Adv. Mater.* **36**, 2408686 (2024).
41. Yang, L. et al. Suppressing halide segregation via pyridine-derivative isomers enables efficient 1.68 eV bandgap perovskite solar cells. *Adv. Mater.* **36**, 2311923 (2024).
42. Scheler, F. et al. Correlation of band bending and ionic losses in 1.68 eV wide band gap perovskite solar cells. *Adv. Energy Mater.* **15**, 2408686 (2025).
43. Ye, Q. et al. Suppressing charge recombination in a methylammonium-free wide-bandgap perovskite film for high-performance and stable perovskite solar cells. *Energy Environ. Sci.***17**, 5866-5875 (2024).

44. Li, M. et al. Hydrogen-bonding-facilitated dimethylammonium extraction for stable and efficient CsPbI3 solar cells with environmentally benign processing. *Joule* **7**, 2595-2608 (2023).
45. Ma, Q. et al. One-step dual-additive passivated wide-bandgap perovskites to realize 44.72%-efficient indoor photovoltaics. *Energy Environ. Sci.* **17**, 1637-1644 (2024).
46. Perdew, J., Burke, p. & Ernzerhof, K. Generalized gradient approximation made simple. *Phys. Rev. Lett.* **77**, 3865 (1996).
48. Grimme, S., Antony, J., Ehrlich, S. & Krieg, H. A consistent and accurate ab initio parametrization of density functional dispersion correction (DFT-D) for the 94 elements H-Pu. *J. Chem. Phys.* **132**, 154104 (2010).
49. Bhardwaj, K. S. et al. Investigating the performance of mixed cation mixed halide-based perovskite solar cells using various hole-transport materials by numerical simulation. *Opt. Quantum Electron.* **53**, 602 (2021).